

Modeling Shear Flow in Rayleigh–Bénard Convection

by

Jean-Luc Thiffeault, B.S.

THESIS

Presented to the Faculty of the Graduate School
of The University of Texas at Austin
in Partial Fulfillment
of the Requirements
for the Degree of

Master of Arts

The University of Texas at Austin

August 1995

A mes parents, Irène et Claude,
sans qui je ne serais pas où je suis,
et à Tara, pour sa patience.

Acknowledgments

I am very grateful to my advisor, Wendell Horton, for his guidance and insight. I also owe thanks to Neil Balmforth, John Bowman, Brad Shadwick, and especially Philip Morrison for their useful comments and gentle criticism.

Abstract

Modeling Shear Flow in Rayleigh–Bénard Convection

by

Jean-Luc Thiffeault, M.A.

The University of Texas at Austin, 1995

Supervisor: C. Wendell Horton, Jr.

The Partial Differential Equations (PDE's) for Rayleigh–Bénard convection of a fluid between two plates with free boundary conditions are turned into an infinite system of coupled Ordinary Differential Equations (ODE's) by expansion in Fourier modes. Shear flow and variable phase between modes are allowed. A general method is presented to make finite truncations of this system that preserve the invariants of the full PDE's in the ideal limit. These truncations also have the property that they have no unbounded solutions and provide a description of the heat flux that has the correct limiting behaviour in a steady-state.

A particular truncation (containing 7 modes) is selected and is compared to a previous model, the 6-ODE model of Howard and Krishnamurti [1]. Nu-

merical calculations are presented to compare the two truncations and study the effects of shear flow on heat transport.

Table of Contents

List of Figures	vii
Chapter 1. Introduction	1
Chapter 2. Preliminaries	4
2.1 Equations of the Rayleigh–Bénard System	4
2.2 Conserved Quantities in the Ideal Limit	6
Chapter 3. Modal Expansion	9
3.1 Expansion of the System into Normal Modes	9
3.2 Linear Stability of Fluid at Rest	13
3.3 Preservation of Conserved Quantities	14
Chapter 4. The 7-ODE Model	21
4.1 Comparison with 6-ODE Model	21
4.2 Numerical Results	26
4.2.1 Case 1: $\sigma = 10$	29
4.2.2 Case 2: $\sigma = 1$	34
4.2.3 Case 3: $\sigma = 0.1$	34
Chapter 5. Conclusions	42
Appendix	
Appendix A. Proofs for the General Case	45
A.1 Boundedness of Solutions	45
A.2 Heat Flow	48
Bibliography	50
Vita	53

List of Figures

1.1	Geometry of a pair of convection rolls (also known as a <i>convection cell</i>), showing the coordinate system and the definition of L and d . The dashed and solid lines indicate that the rolls are counter-rotating.	2
3.1	Critical Rayleigh numbers R_{cmn} for the first four most unstable modes. For $L < 2.0266$, the mode ($m = 1, n = 1$), corresponding to steady convection of a pair of rolls, goes unstable first. All the curves have a minimum at $R_c = 27/4, L = n\sqrt{2}$	15
3.2	Schematic representation of the modes that must be included in a truncation to preserve the invariants. Each black dot gives the (m, n) coordinates of a mode in the truncation. Given that the modes in A_χ are within the dotted rectangle in (a), then the T_{m0} modes in (b) must be included up to $ m = 2M$, where M is the maximum vertical mode number.	20
4.1	Energy (with $\nu = \kappa = 0$) for (a) the 7-ODE model, and (b) the 6-ODE model of Howard and Krishnamurti (the dashed line is K , the dotted line is U , and the solid line is E). The total energy E is not conserved by the 6-ODE truncation. In these calculations, $L = 2$	23
4.2	(a) Transition to shear flow in 7-ODE model, with $\sigma = 1, r = 3.4$, and $k = 1.2$. The solid line is the χ_{11}^r mode, the long-dashed line is the χ_{21}^i mode, and the dashed line is the χ_{10}^i shear flow mode (whose negative was plotted for relative size comparison). The vertical dotted lines show at what times the snapshots of Figure 4.3 were taken. (b) W (the non-shear flow part of the kinetic energy, solid line), F (the shear flow part of the kinetic energy, short-dashed line), U (the potential energy, dotted line), and E , (the total energy, long-dashed line) for the same transition as in (a).	27
4.3	Contour plots of the stream function χ at different times (see Figure 4.2) showing the tilting of the convection cells, for the 7-ODE model. Contours are every 0.5 units.	28
4.4	Plot of the Nusselt number Nu vs r for the 7 ODE model. The points marked by black dots denote a steady state, the triangles a periodic or quasi-periodic state, and the asterisks a chaotic state. These last two symbols represent the average value of Nu , and the dashed lines show the rms amplitude of oscillations. For this graph, $k = 1.2, \sigma = 10$	30

4.5	Plot of the Nusselt number Nu vs r for the 6-ODE model. The points marked by black dots denote a steady state, the triangles a periodic or quasi-periodic state, and the asterisks a chaotic state. These last two symbols represent the average value of Nu , and the dashed lines show the rms amplitude of oscillations. For this graph, $k = 1.2$, $\sigma = 10$	31
4.6	Plot of $Nu \times r$ vs r for the 6-ODE (dashed line) and the 7-ODE (solid line) models. For this graph, $k = 1.2$, $\sigma = 10$. The dotted line has a slope of 5.05, corresponding to the experimental results for $\sigma = 7$ in [5].	32
4.7	Plot of the Nusselt number Nu vs r for the 7 ODE model. The points marked by black dots denote a steady state, the triangles a periodic or quasi-periodic state, and the asterisks a chaotic state. These last two symbols represent the average value of Nu , and the dashed lines show the rms amplitude of oscillations. For this graph, $k = 1.2$, $\sigma = 1$	35
4.8	Plot of the Nusselt number Nu vs r for the 6-ODE model. The points marked by black dots denote a steady state, the triangles a periodic or quasi-periodic state, and the asterisks a chaotic state. These last two symbols represent the average value of Nu , and the dashed lines show the rms amplitude of oscillations. For this graph, $k = 1.2$, $\sigma = 1$	36
4.9	Plot of $Nu \times r$ vs r for the 6-ODE (dashed line) and the 7-ODE (solid line) models. For this graph, $k = 1.2$, $\sigma = 1$	37
4.10	Plot of the Nusselt number Nu vs r for the 7 ODE model. The points marked by black dots denote a steady state, the triangles a periodic or quasi-periodic state, and the asterisks a chaotic state. These last two symbols represent the average value of Nu , and the dashed lines show the rms amplitude of oscillations. Here, $k = 1.2$, $\sigma = 0.1$	39
4.11	Plot of the Nusselt number Nu vs r for the 6-ODE model. The points marked by black dots denote a steady state, the triangles a periodic or quasi-periodic state, and the asterisks a chaotic state. These last two symbols represent the average value of Nu , and the dashed lines show the rms amplitude of oscillations. Here, $k = 1.2$, $\sigma = 0.1$	40
4.12	Plot of $Nu \times r$ vs r for the 6-ODE (dashed line) and the 7-ODE (solid line) models. Here, $k = 1.2$, $\sigma = 0.1$	41

Chapter 1

Introduction

In a horizontal layer of fluid with fixed higher temperature on the bottom boundary and fixed lower temperature on the top boundary, cellular convective flow occurs for a certain range of Rayleigh number R and Prandtl number σ . This state with mass flow is called Rayleigh–Bénard convection [2, 3]. Such states of Rayleigh–Bénard convection are ubiquitous in nature, occurring in slightly modified form in the atmosphere, the ocean, the earth’s mantle, and in the convection zone of the interior of stars [4].

We will be considering a horizontal fluid layer of depth πd (the π is for mathematical convenience, as we shall see later), with a fixed temperature difference ΔT between the top and bottom of the fluid. Horizontally, the velocity and temperature fields of the fluid are periodic with period λ . The horizontal scale of these cells is comparable with the depth of the layer. A useful parameter to describe the shape of such cells is the dimensionless *aspect ratio*, L , being defined as the ratio of the horizontal length of a cell to the depth of the fluid, so that $\lambda = 2\pi Ld$ (see Figure 1.1). It was originally believed that flows in a finite container should scale as its transverse dimension (i.e., d in Figure 1.1). However, recent experiments have shown that thermal convection in a horizontal layer of fluid heated from below can show motions spanning the largest (horizontal) dimension L of the container [5], known as *shear flows*. The experimental setting precluded any externally imposed shear forces. Hence it must be concluded that

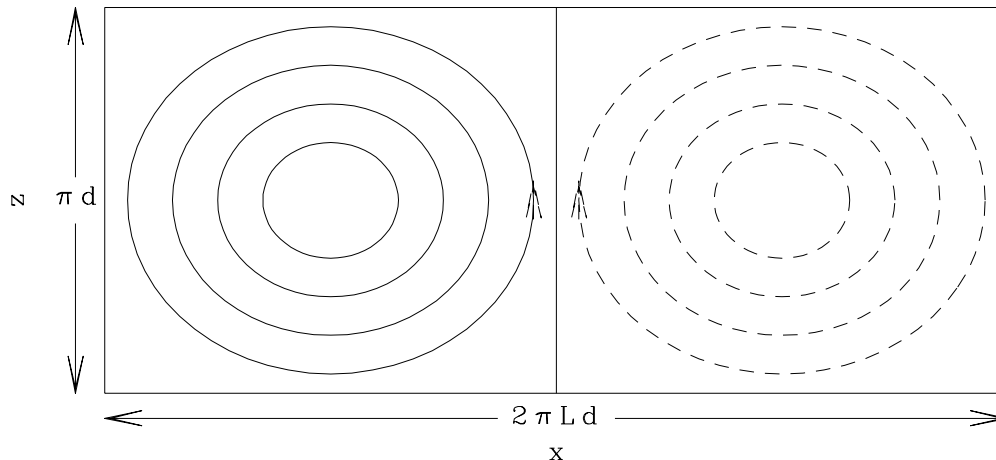


Figure 1.1: Geometry of a pair of convection rolls (also known as a *convection cell*), showing the coordinate system and the definition of L and d . The dashed and solid lines indicate that the rolls are counter-rotating.

these shear flows were driven by a Reynolds stress tensor with non-vanishing horizontal average.

In tokamak plasmas, it is thought that a shear flow in the edge layer is responsible for the so-called H-mode, in which confinement is greatly increased over the normal, or L-mode phase [6]. Convection cells form as a result of the nonlinear development of the Rayleigh–Taylor instability in regions of unfavorable magnetic curvature. Such convection cell turbulence is widely observed in the edge of tokamak plasmas [7]. These vortices can lead to the generation of a shear flow in the same manner as in the Rayleigh–Bénard case [8, 9], and it is believed that this flow creates a barrier to particle transport, thereby greatly improving confinement. Recent experiments have also shown that at higher temperature the appearance of Edge Localized Modes (or ELMs) is observed. The ELMs correspond to a new confinement mode in which oscillations occur in the tokamak edge, and which could be partially explained by the oscillatory shear flow mode that can be destabilized at high enough Rayleigh number.

The method that will be used is known as the *Galerkin* (or *spectral*) method [10].

The chosen basis is the standard Fourier one, because of its great simplicity and the fact that it is especially well-suited to the stress-free boundary conditions (or rather, it is perhaps more honest to say that the stress-free boundary conditions are used because they are especially well-suited to the Fourier basis!). The truncations could help to provide a foundation for turbulence models of L–H transitions such as [11]. One of the major points to be addressed is how to make a truncation have the same invariants as the full PDE's in the dissipationless limit, and whether or not this has any effect on simulations in the strongly dissipative limit.

Chapter 2 is devoted to a presentation of the relevant theory. Section 2.1 is a brief justification of the Boussinesq equations for thermal convection. The preserved quantities of the equations of motion in the dissipationless limit are derived in Section 2.2. In Chapter 3 we use the Galerkin method to expand the stream function and temperature field into a complete set of modes. The set of ODE's obtained by this method is derived in Section 3.1. Section 3.2 addresses the linear stability of the fluid at rest. In Section 3.3, the conditions under which a mode truncation preserves the invariants of the dissipationless PDE's are obtained. Chapter 4 presents a low-order model for shear flow generation, which is an expansion of a model presented in [1]. In Section 4.1 the model is compared with its predecessor, and the advantages are explicitly shown. Section 4.2 compares numerical calculations for the two models. Finally, Chapter 5 is a summary of the arguments of the thesis.

Chapter 2

Preliminaries

In Section 2.1 of this chapter we derive the basic equations that govern Rayleigh–Bénard convection in the Boussinesq approximation. In Section 2.2 we examine the ideal limit of these equations: the case where the viscosity and thermal conductivity are set equal to zero (also called the dissipationless limit). In that regime we demonstrate the conservation of several important quantities (also known as invariants), such as the total energy of the system.

2.1 Equations of the Rayleigh–Bénard System

A fluid heated from below and subject to gravity (the Rayleigh–Bénard convection problem) obeys the set of coupled partial differential equations

$$\begin{aligned}\rho \left(\frac{\partial}{\partial t} + \mathbf{v} \cdot \nabla \right) \mathbf{v} &= -\nabla p + \nu \rho \nabla^2 \mathbf{v} - \rho g \hat{\mathbf{z}}, \\ \left(\frac{\partial}{\partial t} + \mathbf{v} \cdot \nabla \right) \Theta &= \kappa \nabla^2 \Theta,\end{aligned}\tag{2.1}$$

where ρ is the density of the fluid, \mathbf{v} its velocity, p the pressure, ν the kinematic viscosity, $-g\hat{\mathbf{z}}$ the acceleration due to gravity, Θ the temperature, and κ the thermal diffusivity.

The flow is considered slow with respect to the speed of sound waves in the fluid, so that it is taken as incompressible ($\nabla \cdot \mathbf{v} = 0$). In two dimensions (x - z), the velocity

can then be written in terms of a stream function χ as

$$\mathbf{v} = (-\partial_z \chi, \partial_x \chi) = \nabla \chi \times \hat{\mathbf{y}}. \quad (2.2)$$

We shall be using only the x and z dimensions in the rest of this work. This two-dimensionality approximation breaks down at higher Rayleigh number [12].

In the Boussinesq approximation, we take ρ to be constant except in the gravitational force term, where

$$\rho \rightarrow \rho(1 - \alpha(\Theta - \langle \Theta \rangle)). \quad (2.3)$$

The thermal expansion coefficient is denoted here by α , and $\langle \Theta \rangle$ is the average temperature of the fluid in the conduction state, which is characterized by a temperature gradient linear in z and independent of x .

After rescaling the variables to dimensionless form, using the following scales:

$$[x, z] = d, \quad [t] = d^2/\kappa, \quad [\chi] = \kappa, \quad [T] = \nu\kappa/g\alpha d^3, \quad (2.4)$$

Eqs. (2.1) can be written

$$\frac{\partial \nabla^2 \chi}{\partial t} + \{\chi, \nabla^2 \chi\} = \sigma \nabla^4 \chi + \sigma \frac{\partial T}{\partial x}, \quad (2.5)$$

$$\frac{\partial T}{\partial t} + \{\chi, T\} = \nabla^2 T + R \frac{\partial \chi}{\partial x}. \quad (2.6)$$

where χ is the stream function, T is the deviation of the temperature from a linear conduction profile, $\sigma \equiv \nu/\kappa$ is the Prandtl number, and R is the Rayleigh number, defined as

$$R \equiv \frac{g\alpha\Delta T d^3}{\kappa\nu}. \quad (2.7)$$

Here ΔT is the temperature difference between the top and bottom boundaries, and d is the depth of the fluid layer. The Poisson bracket is defined by

$$\{a, b\} \equiv \frac{\partial a}{\partial x} \frac{\partial b}{\partial z} - \frac{\partial b}{\partial x} \frac{\partial a}{\partial z}. \quad (2.8)$$

Equations (2.5) and (2.6) are sometimes referred to as the Boussinesq equations.

There are two major kinds of boundary conditions one can apply at the top and bottom boundaries of the layer. The more physical ones (if the boundaries are actual physical “walls”) are the the no-slip boundary conditions:

$$\chi = \partial_x \chi = \partial_z \chi = T = 0, \quad \text{for } z = 0 \text{ or } \pi d. \quad (2.9)$$

Another set of boundary conditions are the stress-free boundary conditions, where it is required that the walls produce no tangential stresses on the fluid:

$$\chi = \nabla^2 \chi = \partial_x \chi = T = 0, \quad \text{for } z = 0 \text{ or } \pi d. \quad (2.10)$$

The condition $v_z = \partial_x \chi = 0$ at the walls says that the fluid does not penetrate the boundaries. The boundary conditions must be preserved in time, and so using (2.6) and (2.10) we obtain some more constraints:

$$\partial_x T = \nabla^2 T = 0, \quad \text{for } z = 0 \text{ or } d. \quad (2.11)$$

We shall be concerned with boundary conditions (2.10) in this thesis, since they are satisfied naturally by eigenfunctions of the Laplacian operator.

2.2 Conserved Quantities in the Ideal Limit

There are a number of conserved quantities for equations (2.5) and (2.6) in the limit $\nu \rightarrow 0$, $\kappa \rightarrow 0$. We cannot use the scaling given by (2.4), since it involves ν and κ . Instead, we use

$$[x, z] = d, \quad [t] = \sqrt{d/g\alpha\Delta T}, \quad [\chi] = \sqrt{g\alpha\Delta T d^3}, \quad [T] = \Delta T, \quad (2.12)$$

which leads to a new, dissipationless version of (2.5) and (2.6):

$$\frac{\partial \nabla^2 \chi}{\partial t} + \{\chi, \nabla^2 \chi\} = \frac{\partial T}{\partial x}, \quad (2.13)$$

$$\frac{\partial T}{\partial t} + \{\chi, T\} = \frac{\partial \chi}{\partial x}. \quad (2.14)$$

We define two symbols to denote spatial averages:

$$\begin{aligned}\langle A \rangle &\equiv \frac{1}{\pi} \int_0^\pi A dz, \\ \bar{A} &\equiv \frac{1}{2\pi L} \int_0^{2\pi L} A dx,\end{aligned}\tag{2.15}$$

for vertical and horizontal average respectively. The depth of the fluid layer is π , and the system is assumed periodic in the horizontal direction, with length $2\pi Ld$ ($= 2\pi L$ in dimensionless units). The constant L is known as the *aspect ratio* of the system.

If we multiply (2.13) by χ and average over x and z , we get, after some manipulation and use of either set of boundary conditions ((2.9) or (2.10)),

$$\frac{1}{2} \partial_t \langle \overline{(\nabla\chi)^2} \rangle = \langle \overline{T\partial_x\chi} \rangle.\tag{2.16}$$

Now if we multiply (2.14) by z , average over the domain, and manipulate the expression, we obtain

$$\partial_t \langle \overline{zT} \rangle = \langle \overline{T\partial_x\chi} \rangle.\tag{2.17}$$

Subtracting (2.16) and (2.17), we obtain a conservation law:

$$\partial_t \left[\frac{1}{2} \langle \overline{(\nabla\chi)^2} \rangle - \langle \overline{zT} \rangle \right] = 0.\tag{2.18}$$

We define some symbols to represent these quantities. K , U , and E are the kinetic, potential and total energy of the fluid, respectively:

$$K \equiv \frac{1}{2} \langle \overline{(\nabla\chi)^2} \rangle,\tag{2.19}$$

$$U \equiv -\langle \overline{zT} \rangle,\tag{2.20}$$

$$E \equiv K + U.\tag{2.21}$$

Then (2.18) expresses the conservation of total energy in the dissipationless case.

Another invariant is T itself averaged over the domain:

$$\partial_t \langle \overline{T} \rangle = 0. \quad (2.22)$$

If we also multiply (2.14) by T and average over the domain, we obtain

$$\frac{1}{2} \partial_t \langle \overline{T^2} \rangle = \langle \overline{T \partial_x \chi} \rangle, \quad (2.23)$$

which can be combined with (2.16) or (2.17) to yield one more independent conservation law.

The factor $\langle \overline{T \partial_x \chi} \rangle$ which appears in the above equations can be written as $\langle \overline{q_z} \rangle \equiv \langle \overline{T v_z} \rangle$, and it becomes clear that it represents the space-average of the vertical flow of heat, q_z . Finally note that $\langle \overline{T \nabla^2 \chi} \rangle$ is also conserved in the dissipationless limit.

We shall raise the issue in Section 3.3 as to whether a truncation of the system still preserves these invariants.

Chapter 3

Modal Expansion

This chapter is devoted to showing how to turn the Partial Differential Equations (PDE's) of convection into an infinite sequence of coupled Ordinary Differential Equations (ODE's) by expanding the fields into a complete set of normal modes (Section 3.1). In Section 3.2 we go over a linear stability analysis of the fluid at rest. Section 3.3 addresses in detail the question of whether a truncation (a system where only a finite number of modes are retained) preserves the invariants derived in Section 2.2 in the ideal limit.

3.1 Expansion of the System into Normal Modes

To turn the system of partial differential equations (2.5) and (2.6) into ordinary differential equations, we use the following normal mode expansions for the χ and T fields:

$$\chi(x, z, t) = \sum_{m,n} \chi_{mn}(t) e^{i(mz+nkx)}, \quad (3.1)$$

$$T(x, z, t) = \sum_{m,n} T_{mn}(t) e^{i(mz+nkx)}, \quad (3.2)$$

where $k \equiv 1/L$ is the inverse aspect ratio. The two-dimensional domain is

$$(x, z) \in [0, 2\pi L] \times [0, \pi]. \quad (3.3)$$

The summations are over some sets A_χ , A_T of modes (i.e., (m, n) pairs, where both m and n can be negative or zero). If both of these sets are infinite and contain every

possible (m, n) pairs, then the equality holds in (3.1) and (3.2). Otherwise, the expansion is a *truncation* and represents only an approximation to the full system. This expansion is more general than those used in references [13, 14, 15] in two ways: first, it allows for a variable phase in the rolls (by allowing the χ_{mn} 's to be complex) and second, the expansion admits a non-vanishing shear flow part (the χ_{m0} modes).

The complex coefficients in the expansion must satisfy

$$\chi_{mn} = \chi_{-m, -n}^* \quad , \quad T_{mn} = T_{-m, -n}^* \quad . \quad (3.4)$$

in order for the fields to be real (the asterisks denote complex conjugation). The stress-free boundary conditions (2.10) and (2.11) lead to conditions on the χ_{mn} and T_{mn} :

$$\chi_{mn} = -\chi_{m, -n}^* \quad , \quad T_{mn} = -T_{m, -n}^* \quad , \quad (3.5)$$

or equivalently,

$$\begin{aligned} \chi_{0n} &= \chi_{m0}^r = 0, & \chi_{mn}^r &= -\chi_{m, -n}^r, & \chi_{mn}^i &= \chi_{m, -n}^i, \\ T_{0n} &= T_{m0}^r = 0, & T_{mn}^r &= -T_{m, -n}^r, & T_{mn}^i &= T_{m, -n}^i, \end{aligned} \quad (3.6)$$

where the superscripts denote the real part or the imaginary part of χ_{mn} .

For convenience we define ρ_{mn} to be the eigenvalues of the operator $-\nabla^2$:

$$\rho_{mn} \equiv m^2 + k^2 n^2 \quad . \quad (3.7)$$

If we now insert expansions (3.1) and (3.2) into the Boussinesq equations (2.5) and (2.6), we obtain the following set of ODE's:

$$\begin{aligned} \frac{d}{dt} \chi_{mn} &= -\sigma \rho_{mn} \chi_{mn} - i\sigma \frac{k n}{\rho_{mn}} T_{mn} \\ &\quad - k \sum_{m', n'} \sum_{m'', n''} (m' n'' - m'' n') \frac{\rho_{m'' n''}}{\rho_{mn}} \chi_{m' n'} \chi_{m'' n''} \delta_{m'+m'', m} \delta_{n'+n'', n} \quad , \end{aligned} \quad (3.8)$$

$$\begin{aligned} \frac{d}{dt} T_{mn} &= -\rho_{mn} T_{mn} + iR k n \chi_{mn} \\ &\quad - k \sum_{m', n'} \sum_{m'', n''} (m' n'' - m'' n') \chi_{m' n'} T_{m'' n''} \delta_{m'+m'', m} \delta_{n'+n'', n} \quad . \end{aligned} \quad (3.9)$$

The normalization used is that given by (2.4). We are assuming here that if say, χ_{11} is in A_χ , then so are $\chi_{1,-1}$, $\chi_{-1,1}$, and $\chi_{-1,-1}$. But these are not independent by (3.6), so it is possible to turn (3.8) and (3.9) into equations involving sums over only positive indices:

$$\begin{aligned}
\frac{d}{dt}\chi_{mn} &= -\sigma\rho_{mn}\chi_{mn} - i\sigma k n\rho_{mn}^{-1}T_{mn} \\
&\quad - kn\rho_{mn}^{-1}\sum_{p>0}\left(i p\chi_{p0}^i(\theta_{m,p}\rho_{m-p,n}\chi_{|m-p|,n} + \rho_{m+p,n}\chi_{m+p,n})\right. \\
&\quad\quad\quad \left.- i\chi_{pn}(|m-p|\rho_{m-p,0}\chi_{|m-p|,0}^i - (m+p)\rho_{m+p,0}\chi_{m+p,0}^i)\right) \\
&\quad - k\rho_{mn}^{-1}\sum_{p,q>0}\left((pn-mq)\left[\theta_{m,p}\rho_{m-p,n-q}\chi_{pq}\chi_{|m-p|,n-q}\right.\right. \\
&\quad\quad\quad \left.\left.- \rho_{m+p,n+q}\chi_{pq}^*\chi_{m+p,n+q}\right] \right. \\
&\quad\quad\quad \left. - (pn+mq)\left[\theta_{m,p}\rho_{m-p,n+q}\chi_{pq}^*\chi_{|m-p|,n+q}\right.\right. \\
&\quad\quad\quad \left.\left.- \rho_{m+p,n-q}\chi_{pq}\chi_{m+p,n-q}\right]\right), \quad (3.10)
\end{aligned}$$

$$\begin{aligned}
\frac{d}{dt}T_{mn} &= -\rho_{mn}T_{mn} + iRkn\chi_{mn} \\
&\quad - kn\sum_{p>0}\left(i p\chi_{p0}^i(\theta_{m,p}T_{|m-p|,n} + T_{m+p,n})\right. \\
&\quad\quad\quad \left.- i\chi_{pn}(|m-p|T_{|m-p|,0}^i - (m+p)T_{m+p,0}^i)\right) \\
&\quad - k\sum_{p,q>0}\left((pn-mq)\left[\theta_{m,p}\chi_{pq}T_{|m-p|,n-q} - \chi_{pq}^*T_{m+p,n+q}\right] \right. \\
&\quad\quad\quad \left. - (pn+mq)\left[\theta_{m,p}\chi_{pq}^*T_{|m-p|,n+q} - \chi_{pq}T_{m+p,n-q}\right]\right), \quad (3.11)
\end{aligned}$$

where $m, n > 0$. In (3.10) and (3.11) it is understood that following (3.6) any $\chi_{|a|,-|b|}$ is to be converted to $-\chi_{|a|,|b|}^*$, (similarly for the T 's), so that all indices are positive. We have also used the symbol

$$\theta_{a,b} = \begin{cases} 0, & a = b; \\ 1, & a > b; \\ -1, & a < b. \end{cases} \quad (3.12)$$

Equations (3.10) and (3.11) are considerably more opaque than (3.8) and (3.9), but they have the advantage of making the explicit derivation of the nonlinear terms more straightforward by not having to worry about the possible signs of m and n .

For $n = 0$ equations (3.10) and (3.11) simplify to

$$\begin{aligned} \frac{d}{dt} \chi_{m0}^i &= -\sigma m^2 \chi_{m0}^i - 2 k m^{-1} \sum_{p,q>0} q \operatorname{Im} \left[\theta_{m,p} \rho_{m-p,q} \chi_{pq} \chi_{|m-p|,q}^* \right. \\ &\quad \left. - \rho_{m+p,q} \chi_{pq} \chi_{m+p,q}^* \right], \end{aligned} \quad (3.13)$$

$$\begin{aligned} \frac{d}{dt} T_{m0}^i &= -m^2 T_{m0}^i \\ &\quad - 2 k m \sum_{p,q>0} q \operatorname{Im} \left[\theta_{m,p} \chi_{pq} T_{|m-p|,q}^* - \chi_{pq} T_{m+p,q}^* \right]. \end{aligned} \quad (3.14)$$

The symbol Im denotes the imaginary part of the square bracket. The real part of χ_{m0} and T_{m0} vanishes by (3.6). Equation (3.13) is the evolution equation for the shear flow modes (i.e., the modes independent of x).

Since we are interested in the transport properties of the system, we define a useful dimensionless quantity called the *Nusselt number*:

$$\begin{aligned} \operatorname{Nu}(z) &\equiv \frac{\text{Rate of heat transport by convection and conduction}}{\text{Rate of heat conduction by the fluid at rest}}, \\ &= 1 + \frac{1}{R} \left(\overline{q_z^{\text{cv}}} + \overline{q_z^{\text{cd}}} \right), \\ &= 1 + \frac{1}{R} \left(\overline{v_z T} + \overline{\hat{\mathbf{z}} \cdot (-\nabla T)} \right). \end{aligned} \quad (3.15)$$

Equation (3.15) also defines the convective and conductive heat transport quantities, q_z^{cv} and q_z^{cd} . Note that since the heat transport cannot be less than the purely conductive state, the Nusselt number must satisfy $\operatorname{Nu} > 1$ for a physical state. The expansions for q_z^{cv} and q_z^{cd} are

$$\overline{q_z^{\text{cv}}}(z) = -8k \sum_{m,n,p>0} n \left(\chi_{mn}^i T_{pn}^r - \chi_{mn}^r T_{pn}^i \right) \sin mz \sin pz, \quad (3.16)$$

$$\overline{q_z^{\text{cd}}}(z) = 2 \sum_{m>0} m T_{m0}^i \cos mz. \quad (3.17)$$

3.2 Linear Stability of Fluid at Rest

If we assume that both χ and T are small (i.e., the fluid is essentially at rest in the conduction state), then (3.10) and (3.11) reduce to (dropping nonlinear terms)

$$\frac{d}{dt}\chi_{mn} = -\sigma\rho_{mn}\chi_{mn} - i\sigma k n \rho_{mn}^{-1} T_{mn} , \quad (3.18)$$

$$\frac{d}{dt}T_{mn} = -\rho_{mn}T_{mn} + iRk n \chi_{mn} . \quad (3.19)$$

Assume that χ_{mn} and T_{mn} grow exponentially with growth rate γ_{mn} . Then (3.18) and (3.19) can be used to get an equation for γ_{mn} :

$$(\gamma_{mn} + \sigma\rho_{mn})(\gamma_{mn} + \rho_{mn}) = \sigma Rk^2 n^2 \rho_{mn}^{-1} . \quad (3.20)$$

We are interested in the unstable case, $\gamma_{mn} > 0$. This will happen when

$$R > \frac{\rho_{mn}^3}{(kn)^2} . \quad (3.21)$$

We thus define the (m, n) (linear) *critical Rayleigh number* R_{cmn} as

$$R_{cmn} \equiv \frac{\rho_{mn}^3}{(kn)^2} = \frac{(m^2 + (kn)^2)^3}{(kn)^2} = L^2 \frac{(m^2 + (n/L)^2)^3}{n^2} \quad (3.22)$$

Note that R_{cmn} is independent of the Prandtl number.

If $n = 0$, R_{cm0} blows up, and so those modes (the shear flow modes) are never linearly unstable: they must grow nonlinearly if they are to grow at all. The modes with $m = 0$ always vanish because of the boundary conditions (2.10).

Equation (3.22) has a minimum at $L = \sqrt{2}n/m$, where¹

$$\min R_{cmn} = \frac{27}{4} m^4 . \quad (3.23)$$

¹If we had chosen a normalization where the fluid depth was d , and not πd , the numerical factor would be $27\pi^4/4$, as in [2], p.36. The normalization we use avoids having a lot of extra π 's in the equations.

The minimum of $R_{c\,mn}$ is independent of m , and so all $m = 1$ modes will be most unstable at the same value of R . Which one goes unstable first will depend on the value of L , as shown in Figure 3.1. The point at which the curves $R_{c\,11}$ and $R_{c\,12}$ cross is

$$L = \sqrt{\frac{4^{1/3} - 1}{4 - 4^{1/3}}} = 2.0266 \dots , \quad (3.24)$$

where the value of the critical R is

$$R_{c\,11} = R_{c\,12} = \frac{27}{4} \frac{1}{(1 - 4^{-1/3})(4^{2/3} - 1)^2} = 7.8969 \dots . \quad (3.25)$$

We shall restrict ourselves to the case where the $(m = 1, n = 1)$ mode goes unstable first, i.e. the case shown in Figure 1.1. This means that when we include χ_{12} and T_{12} , we should make sure that L is less than the value given by (3.24).

It will prove useful to make use of r , a “relative” Rayleigh number, defined as

$$r \equiv \frac{R}{R_{c\,11}} . \quad (3.26)$$

Then the $(1, 1)$ mode goes unstable for $r > 1$.

3.3 Preservation of Conserved Quantities

As we saw in Section 2.2, there are a number of conserved quantities for the Boussinesq system in the dissipationless limit. The question now raised is: can a truncation of the form given by (3.1) and (3.2) still preserve these invariants?

The expansions for K and U are obtained by inserting equations (3.1) and (3.2) into (2.21):

$$K = 2 \sum_{m,n>0} \rho_{mn} |\chi_{mn}|^2 + \sum_{m>0} \rho_{m0} |\chi_{m0}|^2 , \quad (3.27)$$

$$U = -2 \sum_{p>0} \frac{(-1)^p}{p} T_{p0}^i . \quad (3.28)$$

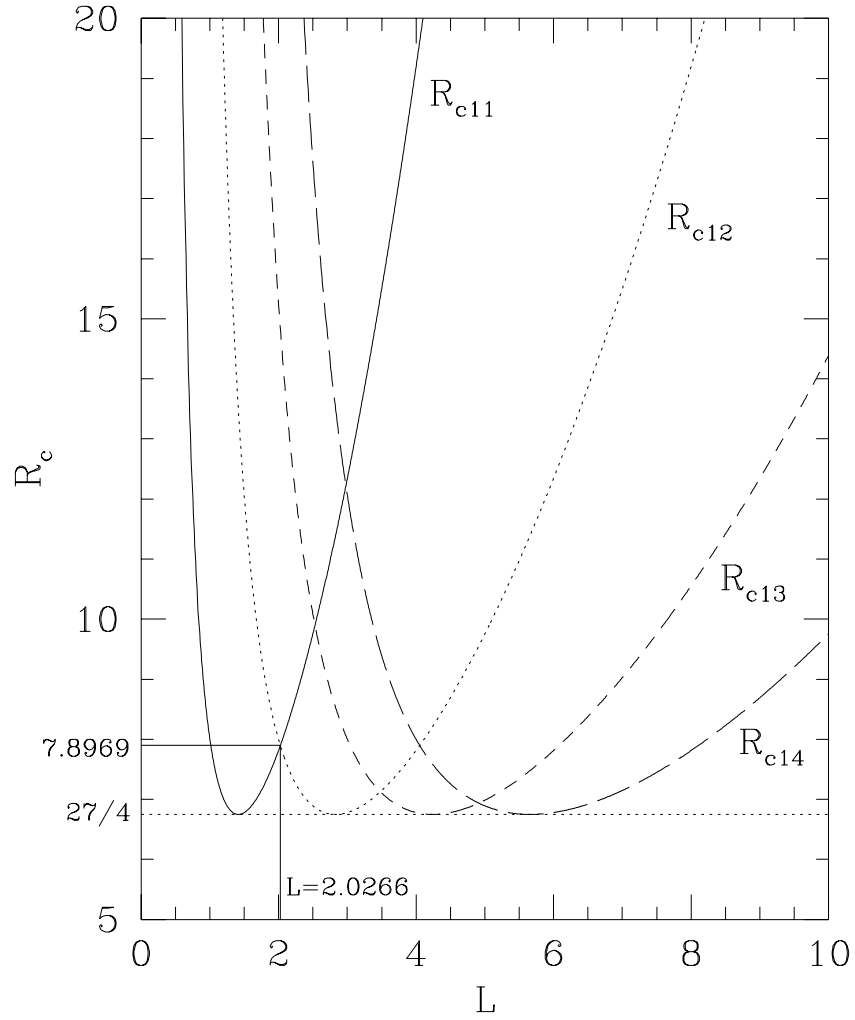


Figure 3.1: Critical Rayleigh numbers R_{cmn} for the first four most unstable modes. For $L < 2.0266$, the mode $(m = 1, n = 1)$, corresponding to steady convection of a pair of rolls, goes unstable first. All the curves have a minimum at $R_c = 27/4$, $L = n\sqrt{2}$.

First we rewrite (3.27) with the m, n sum running over both positive and negative values:

$$K = \frac{1}{2} \sum_{m,n} \rho_{mn} |\chi_{mn}|^2 , \quad (3.29)$$

then we differentiate it with respect to time:

$$\dot{K} = \frac{1}{2} \sum_{m,n} \rho_{mn} \left(\chi_{mn}^* \dot{\chi}_{mn} + \chi_{mn} \dot{\chi}_{mn}^* \right) . \quad (3.30)$$

(The dots denote time derivatives.) From (3.10), we see that we will get a term proportional to

$$\sum_{m,n} \sum_{\substack{m'+m''=m \\ n'+n''=n}} \rho_{m''n''} (m'n'' - m''n') \chi_{mn}^* \chi_{m'n'} \chi_{m''n''} + \text{c.c.} , \quad (3.31)$$

where the sums over the primed and double-primed indices also run over both positive and negative values. We can symmetrize this in terms of m', n' and m'', n'' , and let $m \rightarrow -m$ (also dropping the complex conjugate term):

$$\sum_{\substack{m+m'+m''=0 \\ n+n'+n''=0}} \frac{1}{2} (\rho_{m''n''} - \rho_{m'n'}) (m'n'' - m''n') \chi_{mn} \chi_{m'n'} \chi_{m''n''} , \quad (3.32)$$

We can rewrite this in a clearer way by defining three vectors:

$$\mathbf{k}_1 = (m, n) , \quad \mathbf{k}_2 = (m', n') , \quad \mathbf{k}_3 = (m'', n'') . \quad (3.33)$$

Then (3.32) becomes

$$\sum_{\mathbf{k}_1+\mathbf{k}_2+\mathbf{k}_3=0} \frac{1}{2} (\rho_{\mathbf{k}_3} - \rho_{\mathbf{k}_2}) (\mathbf{k}_2 \times \mathbf{k}_3) \chi_{\mathbf{k}_1} \chi_{\mathbf{k}_2} \chi_{\mathbf{k}_3} . \quad (3.34)$$

We can then completely symmetrize the expression:

$$\begin{aligned} \sum_{\mathbf{k}_1+\mathbf{k}_2+\mathbf{k}_3=0} \frac{1}{6} \left[(\rho_{\mathbf{k}_3} - \rho_{\mathbf{k}_2}) (\mathbf{k}_2 \times \mathbf{k}_3) + (\rho_{\mathbf{k}_2} - \rho_{\mathbf{k}_1}) (\mathbf{k}_1 \times \mathbf{k}_2) \right. \\ \left. + (\rho_{\mathbf{k}_1} - \rho_{\mathbf{k}_3}) (\mathbf{k}_3 \times \mathbf{k}_1) \right] \chi_{\mathbf{k}_1} \chi_{\mathbf{k}_2} \chi_{\mathbf{k}_3} . \quad (3.35) \end{aligned}$$

Since $\mathbf{k}_1 + \mathbf{k}_2 + \mathbf{k}_3 = 0$, the cross products must satisfy

$$\mathbf{k}_1 \times \mathbf{k}_2 = \mathbf{k}_3 \times \mathbf{k}_1, \quad \mathbf{k}_2 \times \mathbf{k}_3 = \mathbf{k}_1 \times \mathbf{k}_2, \quad \mathbf{k}_3 \times \mathbf{k}_1 = \mathbf{k}_2 \times \mathbf{k}_3, \quad (3.36)$$

and hence (3.35) vanishes identically.

Now we are able to write two manageable expressions for \dot{K} and \dot{U} by using (3.8) and (3.14) (in the units given by (2.12), so that we can set ν and κ to zero):

$$\dot{K} = -4k \sum_{m,n>0} n \operatorname{Im} [\chi_{mn} T_{mn}^*], \quad (3.37)$$

$$\begin{aligned} \dot{U} &= 4k \sum_{p,m,n>0} (-1)^p n \theta_{p,m} \operatorname{Im} [\chi_{mn} T_{|m-p|,n}^*] \\ &\quad - 4k \sum_{p',m,n>0} (-1)^{p'} n \operatorname{Im} [\chi_{mn} T_{m+p',n}^*]. \end{aligned} \quad (3.38)$$

The sum of \dot{K} and \dot{U} must vanish for E to be conserved. For that to happen, it must be true that the imaginary parts of the following terms cancel (we divided through by $4k n \chi_{mn}$):

$$\frac{T_{mn}^*}{\boxed{1}} - \sum_{p>0} (-1)^p \theta_{p,m} \frac{T_{|m-p|,n}^*}{\boxed{2}} + \sum_{p'>0} (-1)^{p'} \frac{T_{m+p',n}^*}{\boxed{3}}. \quad (3.39)$$

The term labeled $\boxed{1}$ in (3.39) can only be canceled by a term of $\boxed{2}$, since we cannot have $m = m + p'$ in $\boxed{3}$. Thus, we require $m = |m - p|$, which has a solution $p = 2m$. Then the terms would cancel, since p would be even and $\theta_{p,m} = 1$. Now, assume that $\chi_{mn} = T_{mn} = 0$ for $m > M$, $n \neq 0$. Then the sum over p must run from 1 to $2M$ if it is to cancel $\boxed{1}$ for any value of m and n . So we can rewrite $\boxed{1}$ and $\boxed{2}$ as:

$$\begin{aligned} \boxed{1} + \boxed{2} &= - \sum_{p=1}^{2m-1} (-1)^p \theta_{p,m} T_{|m-p|,n}^* - \sum_{p=2m+1}^{2M} (-1)^p T_{|m-p|,n}^* \\ &= - \left(- \sum_{p=1}^{m-1} (-1)^p T_{|m-p|,n}^* + \sum_{p=m+1}^{2m-1} (-1)^p T_{|m-p|,n}^* \right) \\ &\quad - \sum_{p=2m+1}^{2M} (-1)^p T_{|m-p|,n}^*, \end{aligned} \quad (3.40)$$

We have dropped the $p = m$ term of the sum $\boxed{2}$ since it contains a T_{0n}^* term, which is identically zero by the boundary conditions. In the second sum (the one running from $p = m + 1$ to $p = 2m - 1$) we make the substitution $p = 2m - s$:

$$\begin{aligned} \boxed{1} + \boxed{2} &= - \left(- \sum_{p=1}^{m-1} (-1)^p T_{|m-p|,n}^* + \sum_{s=1}^{m-1} (-1)^s T_{|m-s|,n}^* \right) \\ &\quad - \sum_{p=2m+1}^{2M} (-1)^p T_{|m-p|,n}^* , \\ &= - \sum_{p=2m+1}^{M+m} (-1)^p T_{|m-p|,n}^* , \end{aligned} \quad (3.41)$$

where in the last step we used the fact that $T_{mn}^* = 0$ for $m > M, n \neq 0$, and the sums in the parentheses cancel. If we now let $p = s + 2m$, we obtain:

$$\boxed{1} + \boxed{2} = - \sum_{s=1}^{M-m} (-1)^s T_{m+s,n}^* . \quad (3.42)$$

Sum $\boxed{3}$ over p' also runs from 1 to $2M$, but for $p' > M - m$ the $|m+p'|$ index of $T_{|m+p'|,n}^*$ is greater than M , and so it vanishes. We can finally rewrite (3.39) as:

$$\begin{aligned} \boxed{1} + \boxed{2} + \boxed{3} &= - \sum_{s=1}^{M-m} (-1)^s T_{m+s,n}^* + \sum_{p'=1}^{M-m} (-1)^{p'} T_{m+p',n}^* , \\ &\equiv 0. \end{aligned} \quad (3.43)$$

The recipe for conserving E is then as follows: for a given set of modes A_χ , if M denotes the maximum vertical mode number m in the set, add to A_T all modes of the form $T_{2m,0}^i$, $m = 1, \dots, M$, since that's where we got sums $\boxed{2}$ and $\boxed{3}$ from in (3.39).

The expansion for $\langle \bar{T} \rangle$ is:

$$\langle \bar{T} \rangle = \frac{2}{\pi} \sum_{l \geq 0} \frac{T_{2l+1,0}^i}{2l+1} . \quad (3.44)$$

Taking the time derivative and using (3.14) (in the units given by (2.12)),

$$\frac{d}{dt} \langle \bar{T} \rangle = \frac{4k}{\pi} \sum_{m,n > 0} m \chi_{mn} \operatorname{Im} \left(\sum_{l \geq 0} \theta_{2l+1,m} T_{|2l+1-m|,n}^* - \sum_{l' \geq 0} T_{(2l'+1+m),n}^* \right) \quad (3.45)$$

The sums that must cancel are the imaginary parts of (after dividing (3.45) through by $4mk\chi_{mn}/\pi$):

$$\sum_{p>0 \text{ odd}} \theta_{p,m} T_{|p-m|,n}^* - \sum_{p'>0 \text{ odd}} T_{p'+m,n}^*. \quad (3.46)$$

Cancellation of two terms of the sums requires $|p-m| = p'+m$, with solution $p = p' + 2m$. Then the terms $p' = 1, 3, \dots, M - m$ are canceled by $p = 2m + 1, \dots, M + m$. The terms $p' > M - m$ vanish since then the $p' + m$ index of $T_{p'+m,n}^*$ is greater than M . The terms $p > M + m$ vanish for the same reason. The only terms that remain are the ones with $p = 1, 3, \dots, 2m - 1$, and it is easy to verify that these cancel among themselves (e.g., $p = 1$ with $p = 2m - 1$, etc.) except for $p = m$, which vanishes if m is odd or isn't present in the sum if m is even.

Then the prescription for conserving $\langle \overline{T} \rangle$ is to include in A_T all modes of the form $T_{2l+1,0}$ with $l = 0, 1, \dots, M - 1$. If we include *all* T_{m0} terms, with $m = 1, 2, \dots, 2M$, then both E and $\langle \overline{T} \rangle$ will be conserved by the truncation. This is shown schematically in Figure 3.2. It can be demonstrated that all other invariants of Section 2.2 are also conserved. When a given truncation preserves all those invariants in the dissipationless limits, it will be termed *energy-conserving*. The proof of the preservation of invariants given here is a generalization of the one given [14] to include shear flow and variable phase.

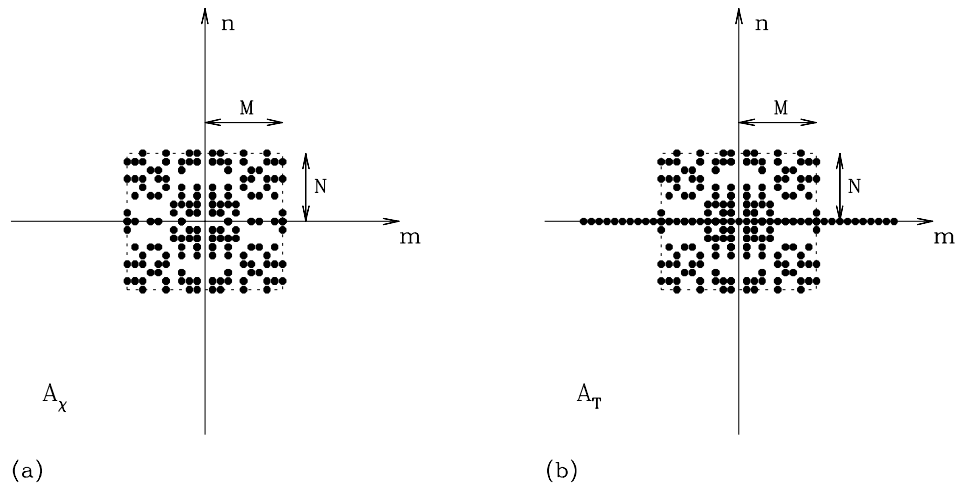


Figure 3.2: Schematic representation of the modes that must be included in a truncation to preserve the invariants. Each black dot gives the (m, n) coordinates of a mode in the truncation. Given that the modes in A_χ are within the dotted rectangle in (a), then the T_{m0} modes in (b) must be included up to $|m| = 2M$, where M is the maximum vertical mode number.

Chapter 4

The 7-ODE Model

This chapter presents a low-order truncation of the Boussinesq equations, retaining only seven modes, following the rules and definitions of Chapter 3. In Section 4.1, we show how the model was derived from its predecessor, the Howard and Krishnamurti 6-mode truncation [1], and justify the addition of the extra mode. Section 4.2 compares numerical calculations for the two models.

4.1 Comparison with 6-ODE Model

The simplest truncation that retains interesting physics is the famous Lorenz model [16]. It consists of retaining the 3 modes:

$$\chi_{11}^r, \quad T_{11}^i, \quad T_{20}^i. \quad (4.1)$$

According to the rules given in Section 3.3, it is energy-conserving, and we also have $\langle \bar{T} \rangle = 0$.

Another popular truncation of the Boussinesq equations is the 6-ODE model given by Howard and Krishnamurti [1, 17]. It includes the 6 modes:

$$\chi_{10}^i, \quad \chi_{11}^r, \quad \chi_{21}^i, \quad T_{11}^i, \quad T_{21}^r, \quad T_{20}^i. \quad (4.2)$$

The Howard and Krishnamurti truncation is the simplest one that allows for a nonzero

shear flow (the χ_{10}^i mode). However, *it is not energy-conserving*. It has a vanishing $\langle \overline{T} \rangle$, but it lacks the T_{40}^i mode to be energy-conserving.

We will add this T_{40}^i mode to the 6-ODE model to obtain what we will call the 7-ODE model. The ODE's for this model are

$$\begin{aligned}
\dot{\chi}_{11}^r &= -\sigma (1 + k^2) \chi_{11}^r + \sigma \frac{k}{1 + k^2} T_{11}^i + k \frac{3 + k^2}{1 + k^2} \chi_{10}^i \chi_{21}^i , \\
\dot{\chi}_{10}^i &= -\sigma \chi_{10}^i - 6k \chi_{11}^r \chi_{21}^i , \\
\dot{\chi}_{21}^i &= -\sigma (4 + k^2) \chi_{21}^i - \sigma \frac{k}{4 + k^2} T_{21}^r - \frac{k^3}{4 + k^2} \chi_{11}^r \chi_{10}^i , \\
\dot{T}_{11}^i &= -(1 + k^2) T_{11}^i + Rk \chi_{11}^r - 2k \chi_{11}^r T_{20}^i - k \chi_{10}^i T_{21}^r , \\
\dot{T}_{20}^i &= -4 T_{20}^i + 4k \chi_{11}^r T_{11}^i , \\
\dot{T}_{21}^r &= -(4 + k^2) T_{21}^r - Rk \chi_{21}^i + k \chi_{10}^i T_{11}^i + 4k \chi_{21}^i T_{40}^i , \\
\dot{T}_{40}^i &= -16 T_{40}^i - 8k \chi_{21}^i T_{21}^r .
\end{aligned} \tag{4.3}$$

The expansions for K and U are (in the units given by (2.4)):

$$\begin{aligned}
K &= 2(1 + k^2) \chi_{11}^r{}^2 + \chi_{10}^i{}^2 + 2(4 + k^2) \chi_{21}^i{}^2 , \\
U &= -\sigma (T_{20}^i + 2T_{40}^i) .
\end{aligned} \tag{4.4}$$

It is straightforward to verify that $E = K + U$ is conserved by (4.3) by first going to the units given by (2.12) and then explicitly substituting (4.3) in \dot{E} (with the dissipation turned off). This is not so with the 6-ODE model. To emphasize this difference, Figure 4.1–(a) shows the numerical results of integrating the 7-ODE model, while in Figure 4.1–(b) we see the results for the unmodified 6-ODE model. The energy is only conserved in the 7-ODE truncation. In fact, the energy is very far from being conserved by the 6-ODE truncation.

The convective and conductive heat flows for the 7-ODE truncation are obtained

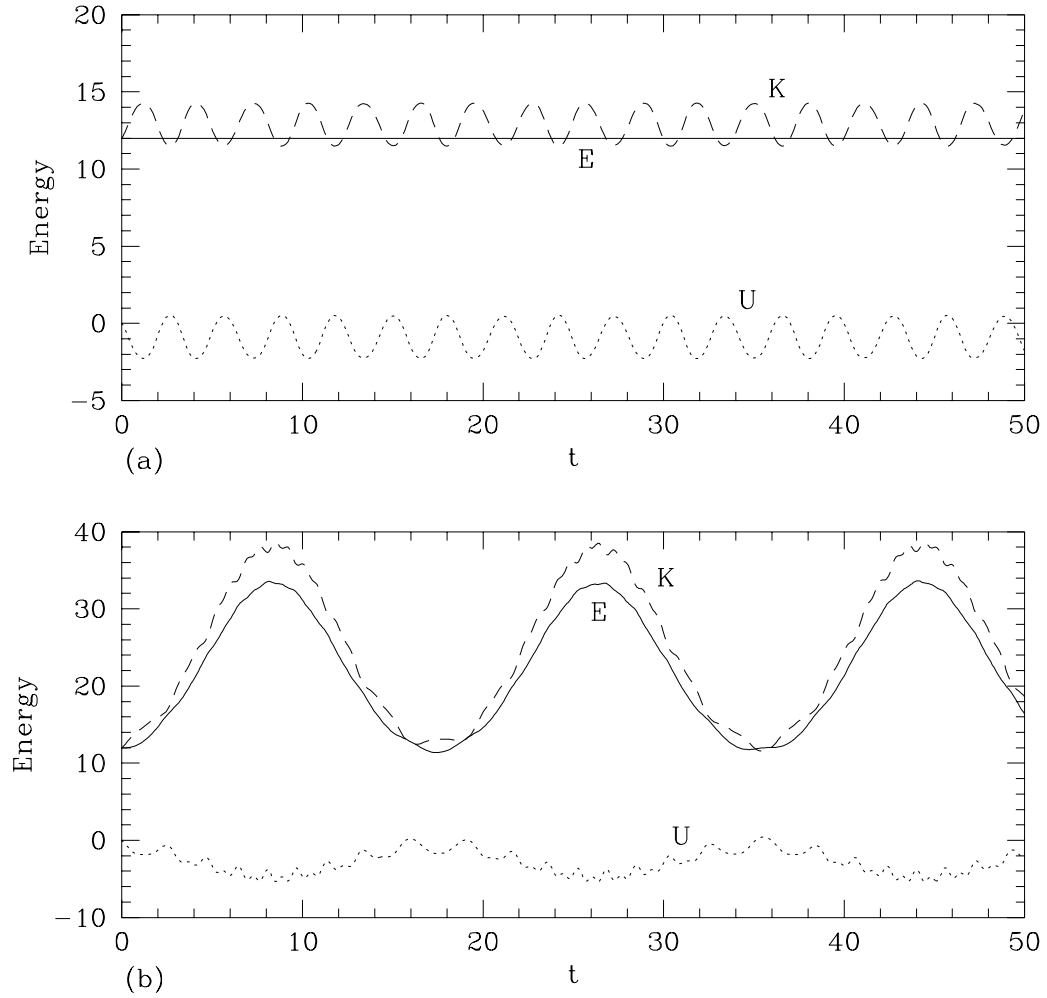


Figure 4.1: Energy (with $\nu = \kappa = 0$) for (a) the 7-ODE model, and (b) the 6-ODE model of Howard and Krishnamurti (the dashed line is K , the dotted line is U , and the solid line is E). The total energy E is not conserved by the 6-ODE truncation. In these calculations, $L = 2$.

from (3.17):

$$\begin{aligned}\overline{q_z^{\text{cv}}}(z) &= 8k \left(\chi_{11}^r T_{11}^i \sin^2 z - \chi_{21}^i T_{21}^r \sin^2 2z \right) , \\ \overline{q_z^{\text{cd}}}(z) &= 4 \left(T_{20}^i \cos 2z + 2T_{40}^i \cos 4z \right) .\end{aligned}\tag{4.5}$$

If we add these together:

$$\begin{aligned}\overline{q_z}(z) &= \overline{q_z^{\text{cv}}} + \overline{q_z^{\text{cd}}} , \\ &= 4k \left(\chi_{11}^r T_{11}^i - \chi_{21}^i T_{21}^r \right) + 4 \left(T_{20}^i - k \chi_{11}^r T_{11}^i \right) \cos 2z \\ &\quad + 4 \left(T_{40}^i + k \chi_{21}^i T_{21}^r \right) \cos 4z , \\ &= \langle \overline{q_z} \rangle - \dot{T}_{20}^i \cos 2z - \frac{1}{2} \dot{T}_{40}^i \cos 4z .\end{aligned}\tag{4.6}$$

If the system reaches a steady state, we expect that the rate of heat transport should be independent of z , i.e., heat cannot “pile up” anywhere in the layer, since this would lead to a time dependency and thus violate the assumption of a steady state. We see this in (4.6), since in a steady state $\dot{T}_{20}^i = \dot{T}_{40}^i = 0$, we would obtain

$$\overline{q_z} = \langle \overline{q_z} \rangle ,\tag{4.7}$$

and so the Nusselt number is independent of z .

In the 6-ODE case, the expression for the heat flux would be

$$\overline{q_z}(z) = \langle \overline{q_z} \rangle - \dot{T}_{20}^i \cos 2z + 4k \chi_{21}^i T_{21}^r \cos 4z ,\tag{4.8}$$

which *is not independent of z in a steady state*. Therefore the flow of energy is not well modeled by the 6-ODE model, *even in the dissipative regime*. Section A.2 of Appendix A proves that all energy-conserving truncations give the correct behaviour of the heat flow for a steady state.

Finally, there is another drawback of the 6-ODE model which the 7-ODE model solves: the boundedness of solutions. To show this, we define a positive definite quantity:

$$Q \equiv \frac{R}{\sigma} \left[2(1+k^2)\chi_{11}^{r\ 2} + 2(4+k^2)\chi_{21}^{i\ 2} + \chi_{10}^{i\ 2} \right] + 2T_{11}^{i\ 2} + 2T_{21}^{r\ 2} + (T_{20}^i - R)^2 + (T_{40}^i - R/2)^2 . \quad (4.9)$$

Note that if Q stays bounded from above, then all the mode variables are bounded from both above and below.

We now take the time derivative of Q , making use of (4.3):

$$\begin{aligned} \frac{d}{dt}Q &= -2 \left\{ 2R(1+k^2)^2 \chi_{11}^{r\ 2} + 2R(4+k^2)^2 \chi_{21}^{i\ 2} + R\chi_{10}^{i\ 2} \right. \\ &\quad \left. + 2(1+k^2)T_{11}^{i\ 2} + 2(4+k^2)T_{21}^{r\ 2} + 2(T_{20}^i - R)^2 + 8(T_{40}^i - R/2)^2 \right\} \\ &\quad - 4T_{20}^{i\ 2} - 16T_{40}^{i\ 2} + 8R^2 . \end{aligned} \quad (4.10)$$

The 7 terms in the curly brackets are each larger or equal to their counterpart in the definition of Q in (4.9). Also, the terms proportional to $T_{20}^{i\ 2}$ and $T_{40}^{i\ 2}$ are strictly negative or zero. We can thus write

$$\frac{d}{dt}Q \leq -2Q + 8R^2 , \quad (4.11)$$

Now if Q is growing, then it must saturate before it reaches $Q \geq 4R^2$, since after that equation (4.11) says that Q must decrease. Thus, Q is bounded from above, and solutions of the 7-ODE model never go to infinity.

In contrast, a similar construction in [1] for the 6-ODE model shows that the modes remain bounded only if $R < R_{c\ 21}$, i.e., if the $(2, 1)$ modes become linearly unstable then they can potentially grow indefinitely. Equation (4.11) shows that this is not so for the 7-ODE model.

Boundedness of the solutions is a physically desirable property, since in real flows one does not observe such singular behaviour. Section A.2 gives a general proof of the boundedness of energy-conserving truncations.

4.2 Numerical Results

We now turn to solving the 7-ODE system (4.3) (and its 6-ODE counterpart) numerically. The integration scheme used is the fourth order Runge-Kutta method with adaptive step size [18]. The absolute accuracy was typically of order 10^{-8} .

Figure 4.2-(a) is a plot of a typical transition to shear flow in the 7-ODE model, for parameter values $r = 3.4$ (corresponding to $R = 34.3$), $\sigma = 1$, $k = 1.2$ (so that $L = 1/k = 0.83333\dots$). This case shows a strong shear flow mode. One can see from the figure that the system first goes on the Lorenz fixed manifold (approximately from $t = 3$ to $t = 14$), but at that value of the Rayleigh number that fixed point is unstable, so the system bifurcates to the other, stable fixed point, with a non-zero shear flow.

To see how the energy transfers to the shear flow modes, we define the quantities W and F by writing

$$\begin{aligned} W &= 2 \sum_{m,n>0} \rho_{mn} |\chi_{mn}|^2 , \\ F &= \sum_{m>0} \rho_{m0} |\chi_{m0}|^2 , \end{aligned} \tag{4.12}$$

so that F represents the kinetic energy contained in the shear flow modes, and W is the energy contained in the remaining (non-shear) modes. For the 7-ODE and 6-ODE models, we have

$$W = 2(1 + k^2) \chi_{11}^r{}^2 + 2(4 + k^2) \chi_{21}^i{}^2$$

and

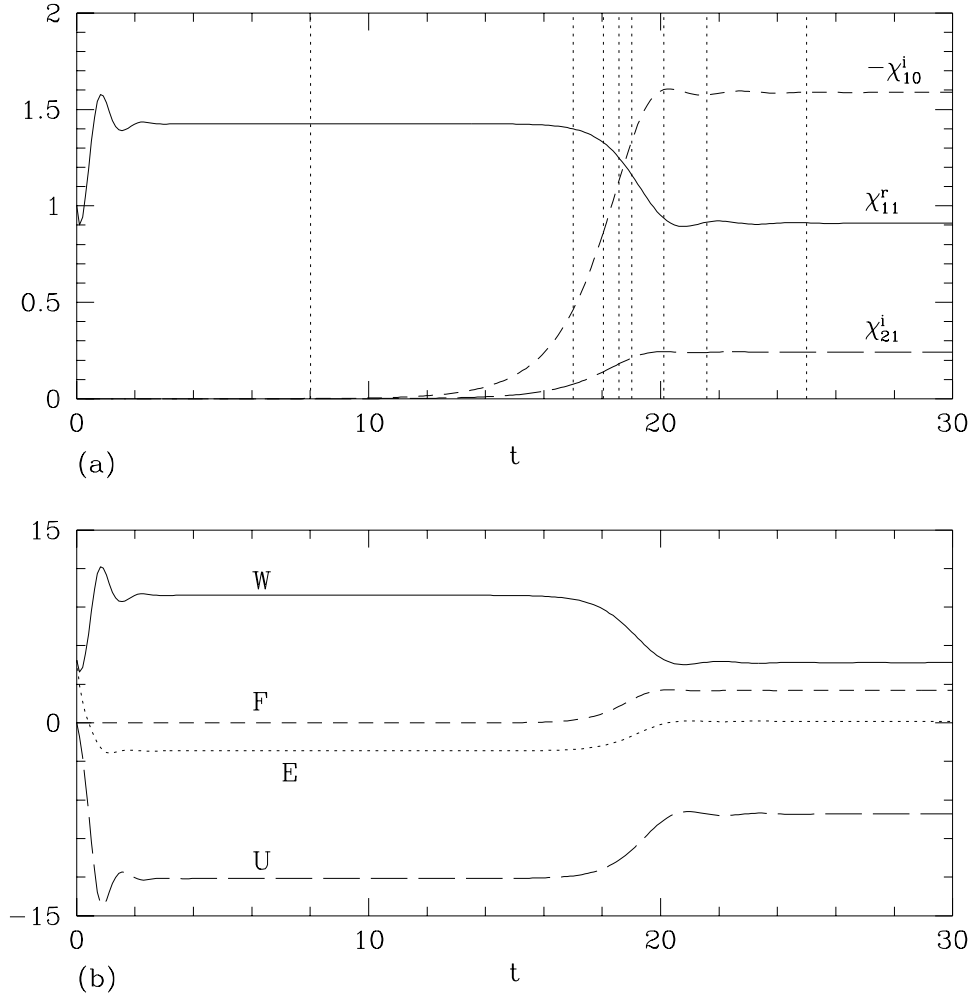


Figure 4.2: (a) Transition to shear flow in 7-ODE model, with $\sigma = 1$, $r = 3.4$, and $k = 1.2$. The solid line is the χ_{11}^r mode, the long-dashed line is the χ_{21}^i mode, and the dashed line is the χ_{10}^i shear flow mode (whose negative was plotted for relative size comparison). The vertical dotted lines show at what times the snapshots of Figure 4.3 were taken. (b) W (the non-shear flow part of the kinetic energy, solid line), F (the shear flow part of the kinetic energy, short-dashed line), U (the potential energy, dotted line), and E , (the total energy, long-dashed line) for the same transition as in (a).

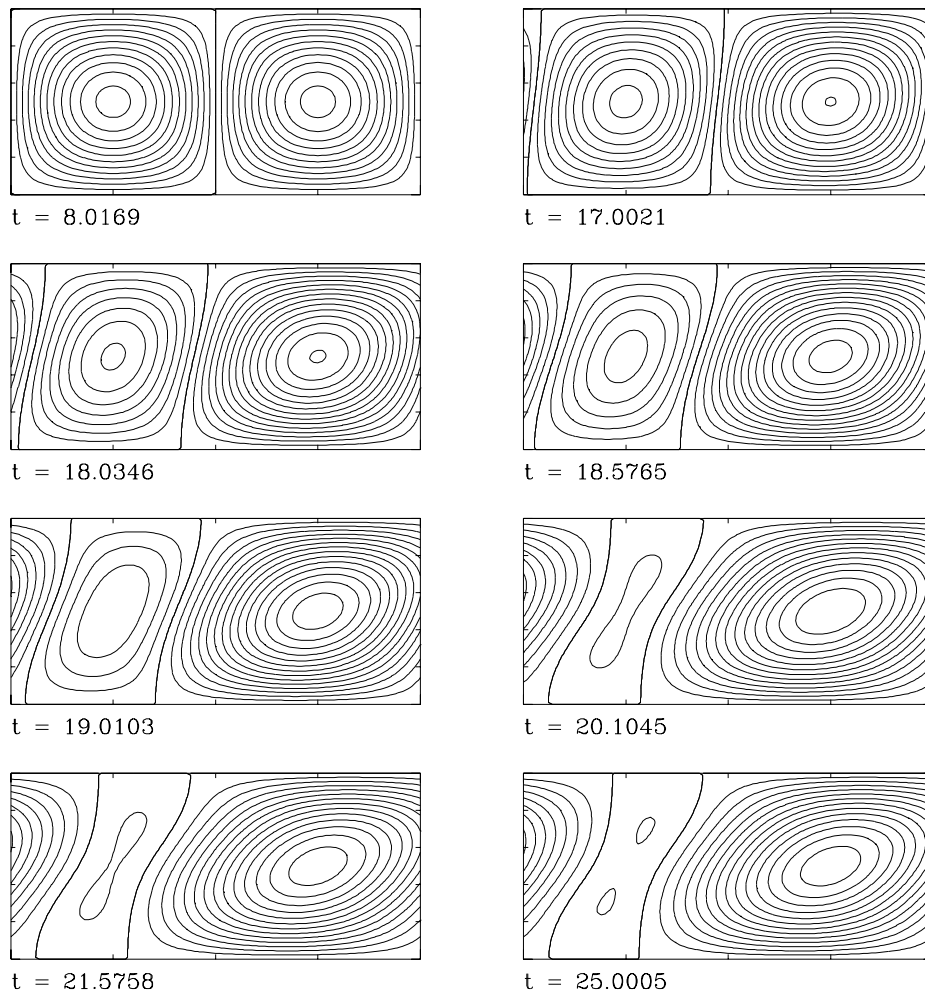


Figure 4.3: Contour plots of the stream function χ at different times (see Figure 4.2) showing the tilting of the convection cells, for the 7-ODE model. Contours are every 0.5 units.

$$F = \chi_{10}^i{}^2. \quad (4.13)$$

Figure 4.2–(b) is a plot of the relevant energies for the same transition as in 4.2–(a). The shear flow mode pumps energy from both the potential and kinetic parts (U and W), and leads to a decrease in the magnitude of the total energy. Figure 4.3 shows contour plots of the stream function at different times throughout the transition, showing clearly the tilting of the convection cells. This effect is observed experimentally [5], and the general appearance of the flow resembles simulations of the full Boussinesq equations [19].

We now study the dependence on r of the Nusselt number for several values of the Prandtl number σ . We shall keep k fixed at 1.2 because the shear flow effect is strong at that number, and to better compare our results with those of [1].

4.2.1 Case 1: $\sigma = 10$

Figure 4.4 shows a plot of the Nusselt number measured at the top of the layer ($z = \pi$) versus the reduced Rayleigh number r . Initially (until about $r \simeq 8.5$) the system is on the Lorenz fixed manifold:

$$\begin{aligned} \chi_{11}^r &= \pm \frac{1}{\sqrt{2}} \frac{1}{1+k^2} \sqrt{R - R_{c11}}, \\ T_{11}^i &= \pm \frac{1}{\sqrt{2}} \frac{1+k^2}{k} \sqrt{R - R_{c11}}, \\ T_{20}^i &= \frac{1}{2} [R - R_{c11}], \end{aligned} \quad (4.14)$$

from which we find for the Nusselt number at $z = \pi$ (using $\overline{q_z^{cd}}$ in (4.5)):

$$\text{Nu} = 3 - \frac{2}{r}. \quad (4.15)$$

Note that this is independent of the Prandtl number. After that point the shear mode becomes unstable and saturates on a new fixed point, accompanied by a sudden *increase*

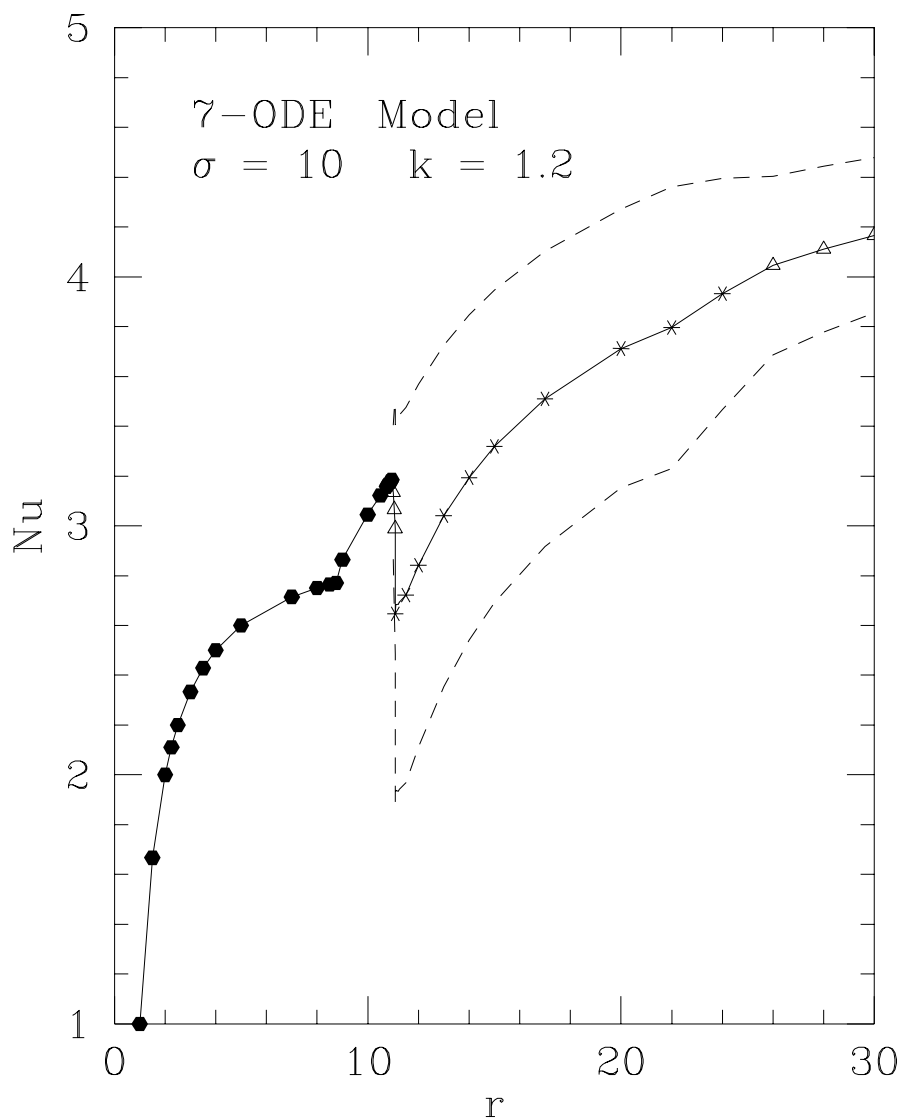


Figure 4.4: Plot of the Nusselt number Nu vs r for the 7 ODE model. The points marked by black dots denote a steady state, the triangles a periodic or quasi-periodic state, and the asterisks a chaotic state. These last two symbols represent the average value of Nu , and the dashed lines show the rms amplitude of oscillations. For this graph, $k = 1.2$, $\sigma = 10$.

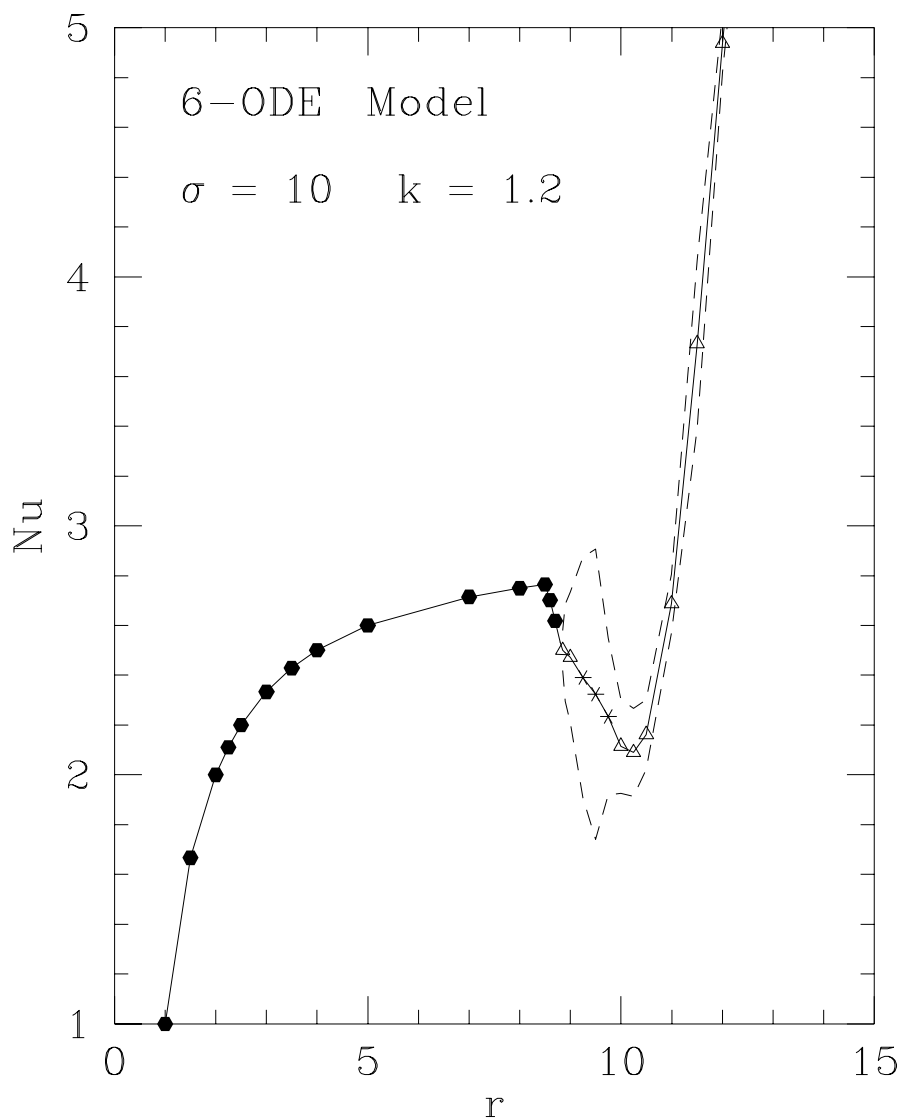


Figure 4.5: Plot of the Nusselt number Nu vs r for the 6-ODE model. The points marked by black dots denote a steady state, the triangles a periodic or quasi-periodic state, and the asterisks a chaotic state. These last two symbols represent the average value of Nu , and the dashed lines show the rms amplitude of oscillations. For this graph, $k = 1.2$, $\sigma = 10$.

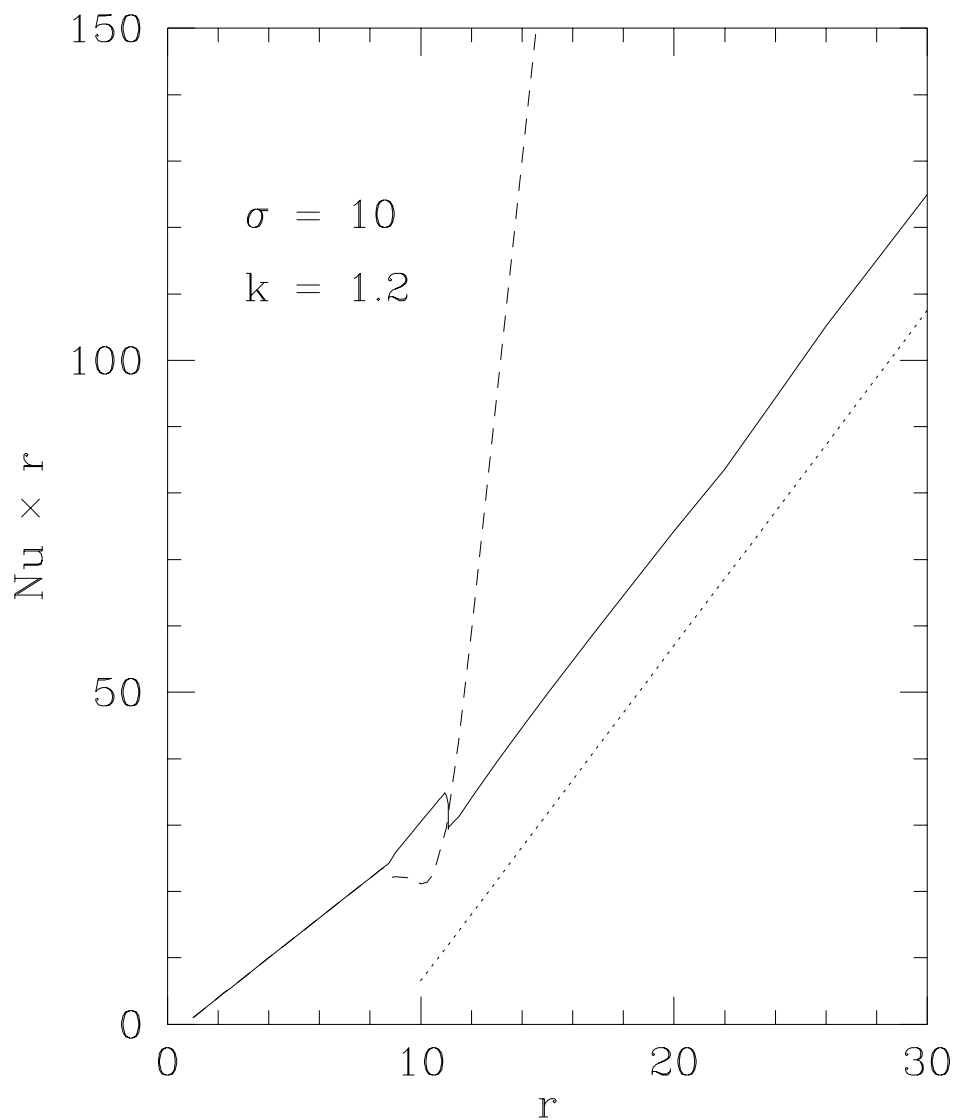


Figure 4.6: Plot of $Nu \times r$ vs r for the 6-ODE (dashed line) and the 7-ODE (solid line) models. For this graph, $k = 1.2$, $\sigma = 10$. The dotted line has a slope of 5.05, corresponding to the experimental results for $\sigma = 7$ in [5].

of the Nusselt number. This goes rather against conventional wisdom, as it is thought that shear flow should inhibit transport. This is also contrary to the 6-ODE model, for which a Nu vs r plot for the same parameter values is shown in Figure 4.5.

At $r \simeq 11$ the 7-ODE model enters a time dependent state, which is initially quasi-periodic but quickly becomes chaotic. The associated decrease in transport might be due to a loss of coherence between the modes due to the time dependence. After that drop, Nu increases steadily. At $r \simeq 25$ it ceases to be chaotic and becomes quasi-periodic again, but the steady rise of Nu is uninterrupted.

In the 6-ODE model, after a period of decreased transport, Nu suddenly shoots up very rapidly. This is no doubt due to the improper saturation of the χ_{21}^i and T_{21}^i modes, which leads to the growth of the T_{20}^i mode. But the 6-ODE model was never intended to be used in that regime, since this is past the point of linear instability of these modes.

Figure 4.6 shows a $\text{Nu} \times r$ versus r plot for both the 7-ODE (solid line) and 6-ODE (dashed line) models. The linear r -dependence of $\text{Nu} \times r$ seen in that figure is predicted by the Lorenz model for low r (by 4.15, $\text{Nu} = 3r - 2$ on the Lorenz fixed manifold). But for larger r , when the system becomes oscillatory, it is surprising to see the linear relation hold for the average value of $\text{Nu} \times r$. This has been observed experimentally [5, 20]. The dotted line in Figure 4.6 is the experimental result for low r of [5] and has a slope of 5.05. The agreement is very good with the 7-ODE model. However, it cannot be concluded that this is anything more than coincidence, since the experiments were done with no-slip boundary conditions, and so the agreement is suspiciously good.

It is seen that the two models behave the same at low r , but quite differently

for larger r , with the 7-ODE model being less chaotic and having a smaller rate of heat transport.

4.2.2 Case 2: $\sigma = 1$

Figure 4.7 shows an analog of Figure 4.4 for the case $\sigma = 1$. After staying at the steady cellular convection fixed point until $r \simeq 2.27$, both the 7-ODE and the 6-ODE models (see Figure 4.8 for the 6-ODE results) undergo a transition to stationary shear flow. The onset of shear flow is now accompanied by a decrease in the Nusselt number for both models, though this decrease is less marked in the 7-ODE model. The 7-ODE model then goes into a quasi-periodic state with a steady rise in Nu, until $r \simeq 15.5$ where it becomes chaotic. It reverts back to quasi-periodicity at $r \simeq 28$. The steady rise in Nu and quasi-periodicity continues until at least $r = 50$.

The 6-ODE model has a similar behaviour, the main difference being a steeper rate of increase of Nu, which continues until at least $r \simeq 50$ (not shown). Figure 4.9 shows the $\text{Nu} \times r$ versus r plot for the two model. It is not immediately obvious that the 7-ODE model has any inherent advantages over the 6-ODE model from these plots, in the absence of direct numerical solutions of the full PDE's for the parameter values.

4.2.3 Case 3: $\sigma = 0.1$

Figure 4.10 shows a Nu vs r plot for the 7-ODE mode, for the case $\sigma = 0.1$. The steady convection fixed point becomes unstable at $r \simeq 1.02$, and the steady shear-flow fixed point becomes unstable shortly after, at $r \simeq 1.11$. The system then stays in a chaotic state until $r \gtrsim 2$. During that stage the Nusselt number is constant (these features are too small to be seen on Figure 4.10). After that point the system becomes quasi-periodic and Nu increases rapidly, with a bifurcation at $r \simeq 17$ and another at $r \simeq 27$.

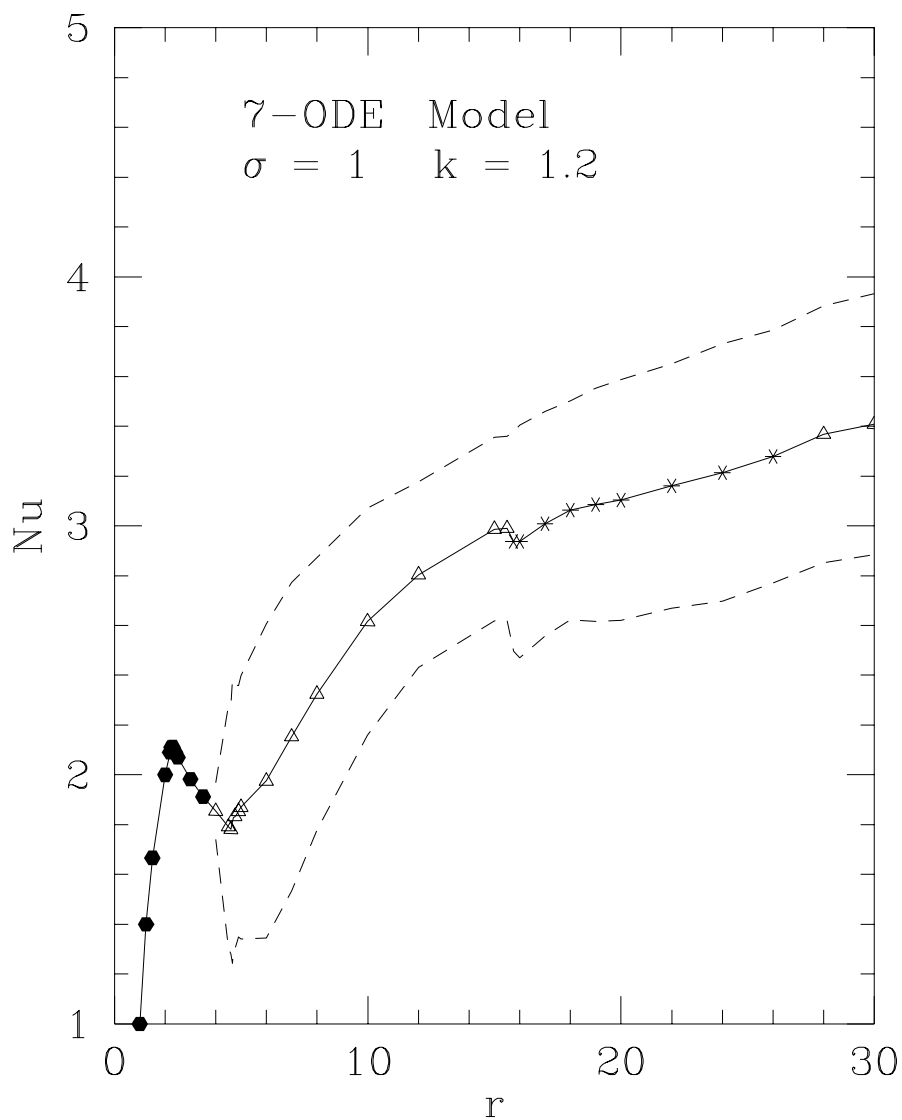


Figure 4.7: Plot of the Nusselt number Nu vs r for the 7 ODE model. The points marked by black dots denote a steady state, the triangles a periodic or quasi-periodic state, and the asterisks a chaotic state. These last two symbols represent the average value of Nu , and the dashed lines show the rms amplitude of oscillations. For this graph, $k = 1.2$, $\sigma = 1$.

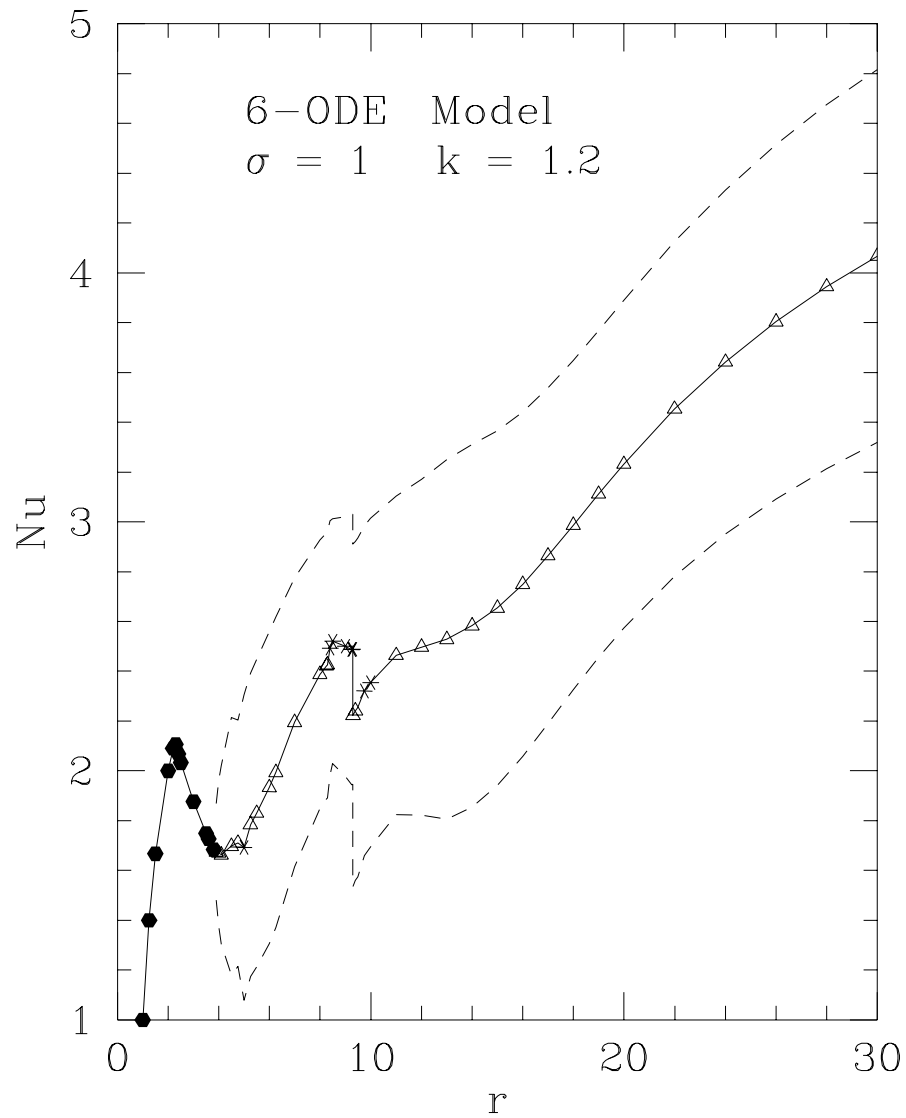


Figure 4.8: Plot of the Nusselt number Nu vs r for the 6-ODE model. The points marked by black dots denote a steady state, the triangles a periodic or quasi-periodic state, and the asterisks a chaotic state. These last two symbols represent the average value of Nu , and the dashed lines show the rms amplitude of oscillations. For this graph, $k = 1.2$, $\sigma = 1$.

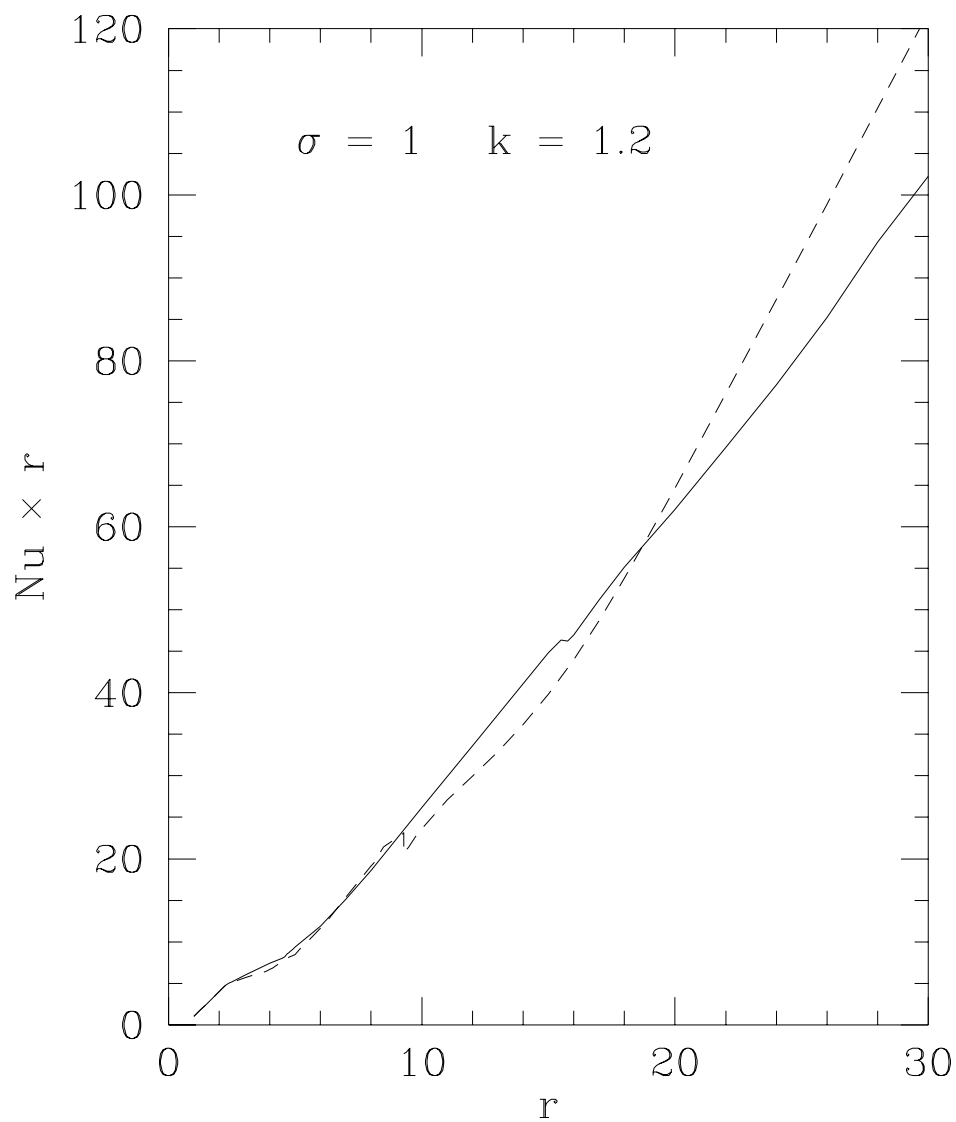


Figure 4.9: Plot of $Nu \times r$ vs r for the 6-ODE (dashed line) and the 7-ODE (solid line) models. For this graph, $k = 1.2$, $\sigma = 1$.

The 6-ODE model results (shown in Figure 4.11) is seen to have one less bifurcation (only one at $r \simeq 13.5$) and to rise slightly less steeply than the 7-ODE model (as seen in Figure 4.12). Note that for both models the quasi-periodic, steady rise continues until at least $r = 90$ (not shown). The oscillations of the 6-ODE model are significantly larger than for the 7-ODE model (by a factor of about 3). Again, for this case it is not immediately obvious that the 7-ODE model has any advantages over the 6-ODE model.

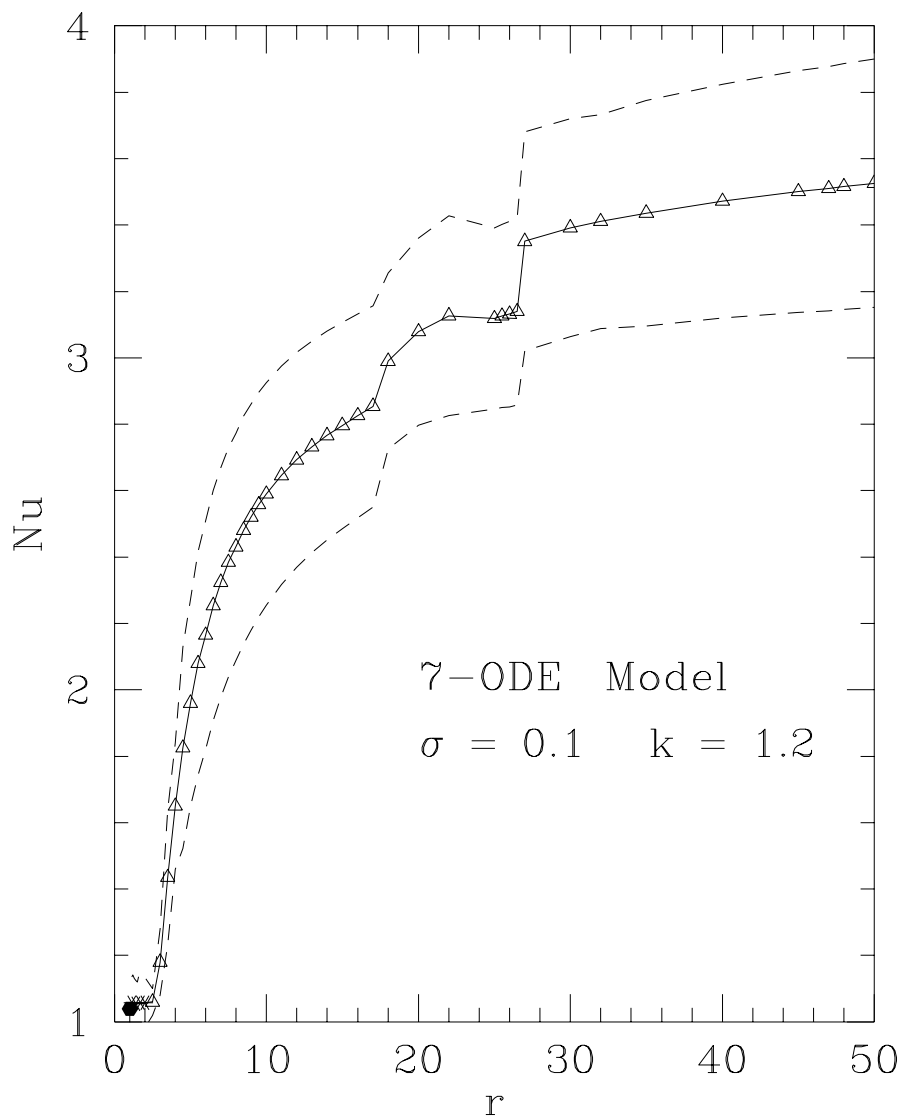


Figure 4.10: Plot of the Nusselt number Nu vs r for the 7 ODE model. The points marked by black dots denote a steady state, the triangles a periodic or quasi-periodic state, and the asterisks a chaotic state. These last two symbols represent the average value of Nu , and the dashed lines show the rms amplitude of oscillations. Here, $k = 1.2$, $\sigma = 0.1$.

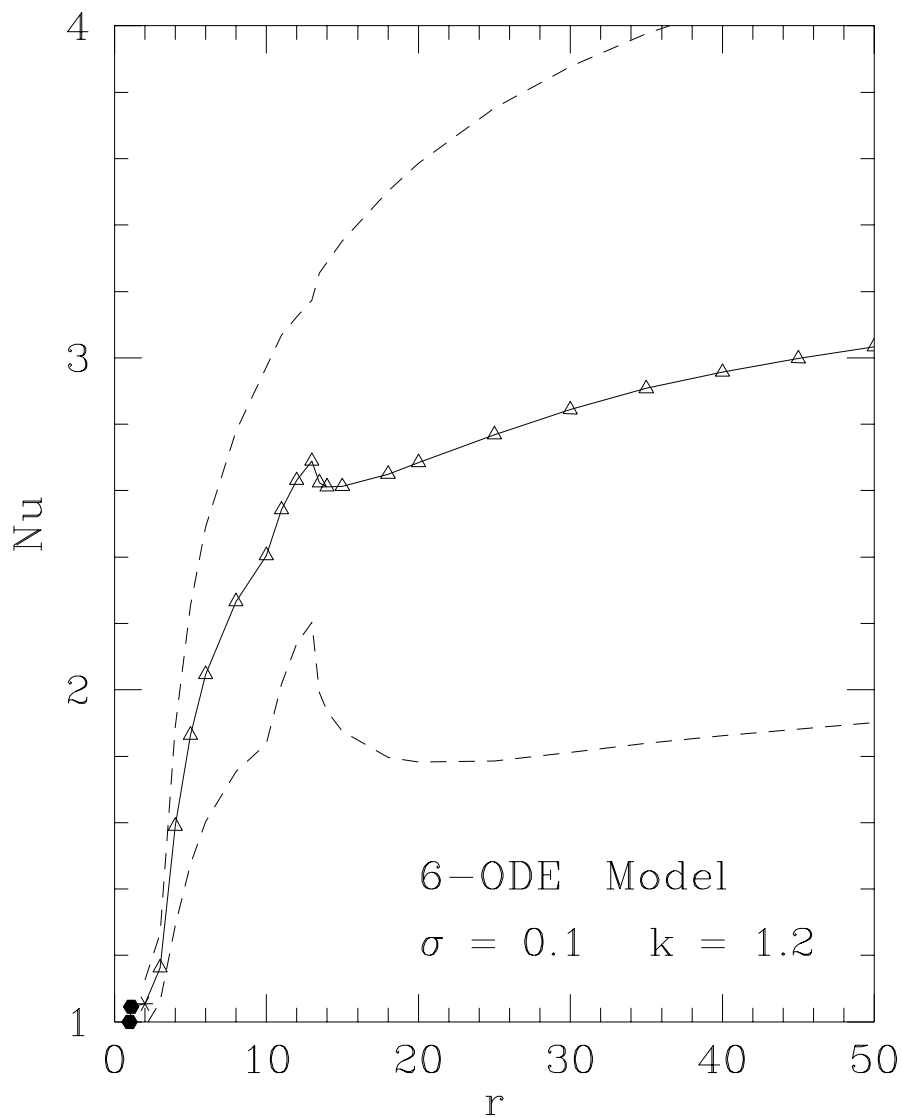


Figure 4.11: Plot of the Nusselt number Nu vs r for the 6-ODE model. The points marked by black dots denote a steady state, the triangles a periodic or quasi-periodic state, and the asterisks a chaotic state. These last two symbols represent the average value of Nu , and the dashed lines show the rms amplitude of oscillations. Here, $k = 1.2$, $\sigma = 0.1$.

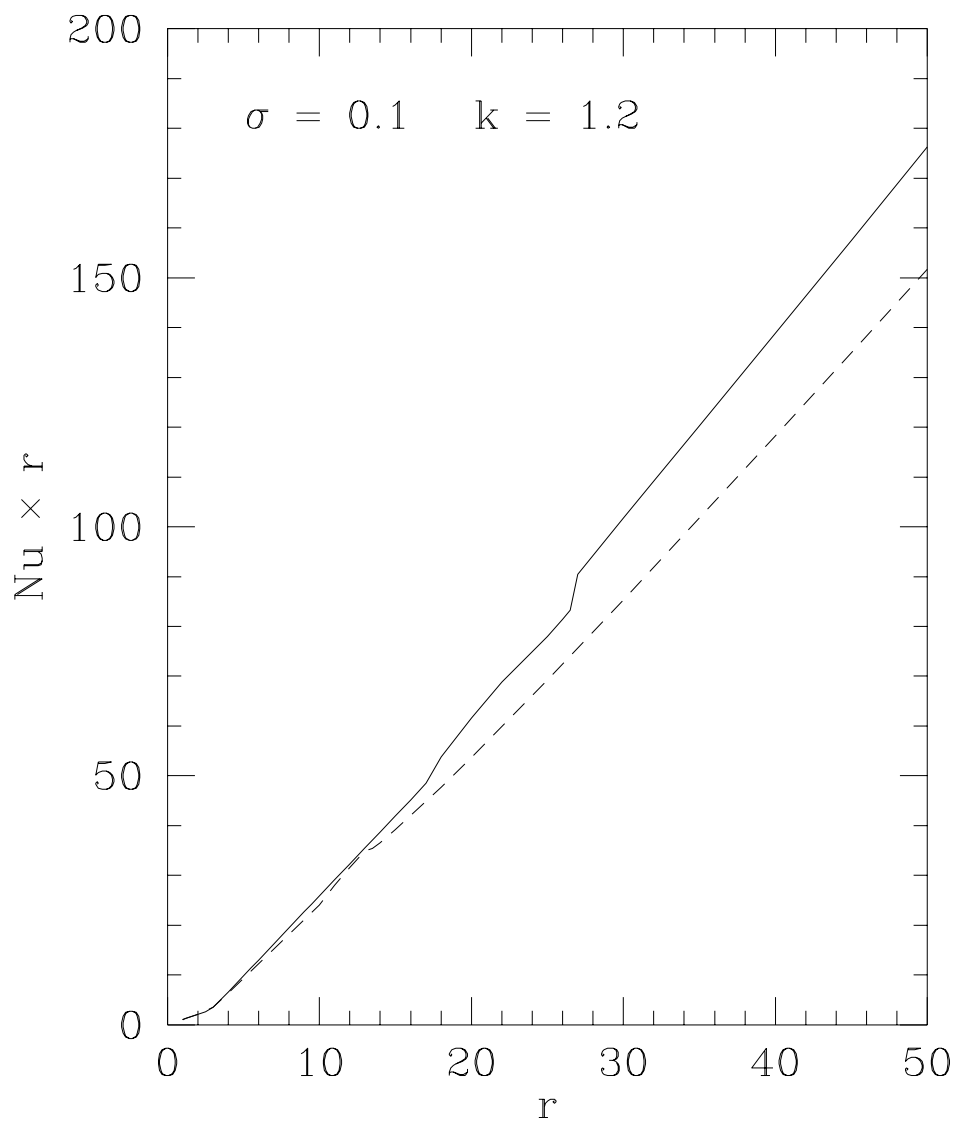


Figure 4.12: Plot of $Nu \times r$ vs r for the 6-ODE (dashed line) and the 7-ODE (solid line) models. Here, $k = 1.2$, $\sigma = 0.1$.

Chapter 5

Conclusions

In this thesis we have developed a general method for generating energy-conserving Galerkin approximations of the PDE's of Rayleigh–Bénard convection. They are more general than [13, 14, 15] because they allow for shear flows (modes independent of the horizontal dimension x) and variable phase of the rolls (breaking point symmetry with respect to the center of the rolls). This was used in some other work by this author (following a suggestion of P. J. Morrison) for a low-order model of chaotic particle transport, in a manner similar to [1] for shear flow and [19, 21, 22] for rolls with time-dependent phase.

There are essentially three arguments for using energy-conserving Galerkin approximations:

The first is simply that they are energy-conserving. Their important property is that the cascade of energy through the inertial range to the dissipation scale is modeled without extraneous terms in the energy equations [14]. This makes them more closely related to the full equations, and so one expects that these approximations are inherently “better”. An argument against this is that in the dissipative regime the system is far from ideal, and so in deciding which modes to include in the truncation it is more important to select terms that approximate the attracting manifold well, and the question of whether energy is conserved by the truncation or not might be of secondary importance [23].

The second property is the proper description of the heat flow in the steady-state limit, even with dissipation. This is important for essentially the same reasons as the previous argument, except that this argument doesn't suffer from the criticism of being a valid property only in the ideal limit. In Section A.2 of Appendix A it is shown that all energy-conserving truncations have this correct behaviour of the heat flow in a steady-state.

The third argument is the boundedness of solutions. In Section A.1 the boundedness of solutions for general energy-conserving Galerkin approximations is shown. This point is a strong one, since the infinite solutions are definitely unphysical, and the truncation is then closer to the full solution in a least this respect.

The numerical results for the comparison of the two models are conclusive only in the higher Prandtl number case ($\sigma = 10$) where the 6-ODE solution grows too fast compared to experimental result (if it is to be trusted that numerical results for different boundary conditions can be trusted). For the other values of the Prandtl number the two models behave differently, but in the absence of numerical solutions of the full equations it cannot be concluded that one is better than the other. The most noticeable difference is that the oscillations for the 7-ODE model tend to be smaller, especially at low Prandtl number. It has thus at least been established that the addition of the extra mode affects the solution significantly, and in particular for $\sigma = 10$ the two models disagree about the way that shear flow affects heat transport.

Appendix

Appendix A

Proofs for the General Case

In this Appendix we present the general case of the proofs given specifically for the 7-ODE model in Section 4.1. Section A.1 gives the proof of boundedness, and Section A.2 shows that the total heat flow is independent of z for a steady-state. Both these properties hold if the truncation is energy-conserving.

A.1 Boundedness of Solutions

To show that the solutions to the system of ODE's (3.10) and (3.11) remain bounded for all times, we consider the kinetic energy K defined previously:

$$K = 2 \sum_{m,n>0} \rho_{mn} |\chi_{mn}|^2 + \sum_{m>0} \rho_{m0} |\chi_{m0}|^2, \quad (\text{A.1})$$

and a quantity which we will call V :

$$V \equiv 2 \sum_{m,n>0} |T_{mn}|^2 + \sum_{m>0} \left(T_{m0}^i - \frac{2R}{m} \right)^2. \quad (\text{A.2})$$

Recall that $\rho_{mn} = m^2 + k^2 n^2$. We then construct a generalization of Q from Section 4.1 for an arbitrary number of modes:

$$\begin{aligned} Q &\equiv \frac{R}{\sigma} K + V \\ &= 2 \frac{R}{\sigma} \sum_{m,n>0} \rho_{mn} |\chi_{mn}|^2 + \frac{R}{\sigma} \sum_{m>0} \rho_{m0} |\chi_{m0}|^2 \\ &\quad + 2 \sum_{m,n>0} |T_{mn}|^2 + \sum_{m>0} \left(T_{m0}^i - \frac{2R}{m} \right)^2. \end{aligned} \quad (\text{A.3})$$

If any mode goes to infinity, Q will go to infinity. It includes all of the modes, and it is non-negative. Hence, Q being bounded from above is a necessary and sufficient condition for the boundedness of all solutions.

Using (3.10) to take the time derivative of K , we have already seen in Section 3.3 that the triplet terms of the form $\chi_{mn}\chi_{m'n'}\chi_{m''n''}$ cancel each other, and we are left with

$$\begin{aligned} \frac{d}{dt}K &= -4\sigma \sum_{m,n>0} \rho_{mn}^2 |\chi_{mn}|^2 - 2\sigma \sum_{m>0} \rho_{m0}^2 |\chi_{m0}|^2 \\ &\quad - 4k\sigma \sum_{m,n>0} n \operatorname{Im} \chi_{mn} T_{mn}^* \end{aligned} \quad (\text{A.4})$$

Now we take the time derivative of V using (3.11). The triplet terms of the form $\chi_{mn}T_{m'n'}T_{m''n''}$ can be shown to cancel in a manner analogous to the $\chi_{mn}\chi_{m'n'}\chi_{m''n''}$ triplets in Section 3.3, and we have

$$\begin{aligned} \frac{d}{dt}V &= -4 \sum_{m,n>0} \rho_{mn} |T_{mn}|^2 - 2 \sum_{m>0} m^2 T_{m0}^i \left(T_{m0}^i - \frac{2R}{m} \right) - 4kR \sum_{p,q>0} q \operatorname{Im} \chi_{pq} T_{pq}^* \\ &\quad + 8kR \sum_{p,q>0} q \operatorname{Im} \left[\chi_{pq} \sum_{m>0} \theta_{m,p} T_{|m-p|,q}^* - \chi_{pq} \sum_{m'>0} T_{m'+p,q}^* \right]. \end{aligned} \quad (\text{A.5})$$

The symbol $\theta_{m,n}$ was defined to be the sign of $m - n$, and vanishes if $m = n$. We concentrate on the two sums in the square bracket (factoring out a χ_{pq}):

$$\mathcal{A}_{pq} \equiv \sum_{m>0} \theta_{m,p} T_{|m-p|,q}^* - \sum_{m'>0} T_{m'+p,q}^*. \quad (\text{A.6})$$

We separate the first sum into two parts, allowing us to eliminate the $\theta_{m,p}$'s:

$$\mathcal{A}_{pq} = - \sum_{m=1}^{p-1} T_{|m-p|,q}^* + \sum_{m=p+1}^{M+p} T_{|m-p|,q}^* - \sum_{m'=1}^{M-p} T_{m'+p,q}^*, \quad (\text{A.7})$$

and relabel:

$$\mathcal{A}_{pq} = - \sum_{r=1}^{p-1} T_{rq}^* + \sum_{s=1}^M T_{sq}^* - \sum_{v=p+1}^M T_{vq}^*. \quad (\text{A.8})$$

The we combine the first and third sums, adding the $r = p$ term that's missing:

$$\mathcal{A}_{pq} = T_{pq}^* - \sum_{r=1}^M T_{rq}^* + \sum_{s=1}^M T_{sq}^* = T_{pq}^*. \quad (\text{A.9})$$

Equation (A.5) thus simplifies to:

$$\begin{aligned} \frac{d}{dt}V &= -4 \sum_{m,n>0} \rho_{mn} |T_{mn}|^2 - 2 \sum_{m>0} m^2 T_{m0}^i \left(T_{m0}^i - \frac{2R}{m} \right) \\ &\quad + 4kR \sum_{p,q>0} q \operatorname{Im} \chi_{pq} T_{pq}^* . \end{aligned} \quad (\text{A.10})$$

Using (A.4) and (A.10) in (A.3), we find

$$\begin{aligned} \frac{d}{dt}Q &= \frac{R}{\sigma} \dot{K} + \dot{V} \\ &= -4R \sum_{m,n>0} \rho_{mn}^2 |\chi_{mn}|^2 - 2R \sum_{m>0} \rho_{m0}^2 |\chi_{m0}|^2 \\ &\quad - 4 \sum_{m,n>0} \rho_{mn} |T_{mn}|^2 - 2 \sum_{m>0} m^2 T_{m0}^i \left(T_{m0}^i - \frac{2R}{m} \right) . \end{aligned} \quad (\text{A.11})$$

The last summand can be rewritten:

$$\begin{aligned} -2m^2 T_{m0}^i \left(T_{m0}^i - \frac{2R}{m} \right) &= -m^2 T_{m0}^i{}^2 - m^2 \left(T_{m0}^i{}^2 - \frac{4R}{m} T_{m0}^i \right) \\ &= -m^2 T_{m0}^i{}^2 - m^2 \left(T_{m0}^i - \frac{2R}{m} \right)^2 + 4R^2 , \end{aligned} \quad (\text{A.12})$$

so that (A.11) becomes:

$$\begin{aligned} \frac{d}{dt}Q &= -4R \sum_{m,n>0} \rho_{mn}^2 |\chi_{mn}|^2 - 2R \sum_{m>0} \rho_{m0}^2 |\chi_{m0}|^2 \\ &\quad - 4 \sum_{m,n>0} \rho_{mn} |T_{mn}|^2 - \sum_{m>0} m^2 \left(T_{m0}^i - \frac{2R}{m} \right)^2 \\ &\quad - \sum_{m>0} m^2 T_{m0}^i{}^2 + 4M_0 R^2 , \end{aligned} \quad (\text{A.13})$$

where M_0 is the number of T_{m0} modes included in the truncation. Comparing the first four terms of (A.13) with their counterpart in (A.3), we find can write:

$$\frac{d}{dt}Q \leq -\min\{1, 2\sigma\}Q - \sum_{m>0} m^2 T_{m0}^i{}^2 + 4M_0 R^2 , \quad (\text{A.14})$$

and since $m^2 T_{m0}^i{}^2 \geq 0$,

$$\frac{d}{dt}Q \leq -\min\{1, 2\sigma\}Q + 4M_0 R^2 . \quad (\text{A.15})$$

Thus, for

$$Q > \frac{4M_0 R^2}{\min\{1, 2\sigma\}}, \quad (\text{A.16})$$

Q must decrease. Hence Q is bounded from above, and so all the modes must be bounded from above and below.

In the dissipationless limit ($\nu = \kappa = 0$), after changing to units (2.12), we would obtain

$$\frac{d}{dt}Q = 0, \quad (\text{A.17})$$

so that the system is also bounded in the dissipationless limit since the initial conditions must be finite.

A.2 Heat Flow

The expansions for the x -averaged convective and conductive vertical heat flows $\overline{q_z^{\text{cv}}}$ and $\overline{q_z^{\text{cd}}}$ are given in Section 3.1:

$$\overline{q_z^{\text{cv}}}(z) = -8k \sum_{p,q>0} q \sum_{m>0} \text{Im} \chi_{pq} T_{mq}^* \sin mz \sin pz, \quad (\text{A.18})$$

$$\overline{q_z^{\text{cd}}}(z) = 2 \sum_{m>0} m T_{m0}^i \cos mz. \quad (\text{A.19})$$

Using (3.14), we can rewrite (A.19) as

$$\begin{aligned} \overline{q_z^{\text{cd}}}(z) &= -2 \sum_{m>0} \frac{T_{m0}^i}{m} \cos mz - 4k \sum_{p,q>0} q \sum_{m>0} \theta_{m,p} \text{Im} \chi_{pq} T_{|m-p|,q}^* \cos mz \\ &\quad + 4k \sum_{p,q>0} q \sum_{m'>0} \text{Im} \chi_{pq} T_{m'+p,q}^* \cos m'z. \end{aligned} \quad (\text{A.20})$$

If we concentrate on the sums over m and m' in (A.20), we can write

$$\mathcal{B}_{pq} \equiv \sum_{m=1}^{M+p} \theta_{m,p} T_{|m-p|,q}^* \cos mz - \sum_{m'=1}^{M-p} T_{m'+p,q}^* \cos m'z. \quad (\text{A.21})$$

We have limited the upper bound of the sums to the cases where the z index of the T 's is less than or equal to M , since beyond that the modes vanish (since $q > 0$). Now we

separate the first sum into two parts, one with $m < p$, the other with $m > p$:

$$\mathcal{B}_{pq} = - \sum_{m=1}^{p-1} T_{|m-p|,q}^* \cos mz + \sum_{m=p+1}^{M-p} T_{|m-p|,q}^* \cos mz - \sum_{m'=1}^{M-p} T_{m'+p,q}^* \cos m'z . \quad (\text{A.22})$$

We relabel the sums such that $r = p - m$, $s = m - p$, and $v = m' + p$:

$$\mathcal{B}_{pq} = - \sum_{r=1}^{p-1} T_{rq}^* \cos(p-r)z + \sum_{s=1}^M T_{sq}^* \cos(p+s)z - \sum_{v=p+1}^M T_{vq}^* \cos(p-v)z , \quad (\text{A.23})$$

then we combine the r and v sums, adding the $\chi_{pq} T_{pq}^*$ term necessary to complete it:

$$\begin{aligned} \mathcal{B}_{pq} &= \chi_{pq} T_{pq}^* - \sum_{r=1}^M T_{rq}^* \cos(p-r)z + \sum_{s=1}^M T_{sq}^* \cos(p+s)z \\ &= \chi_{pq} T_{pq}^* - \sum_{r=1}^M T_{rq}^* (\cos(p-r)z - \cos(p+r)z) \\ &= \chi_{pq} T_{pq}^* - 2 \sum_{m=1}^M T_{mq}^* \sin mz \sin pz . \end{aligned} \quad (\text{A.24})$$

In the last step we changed the dummy index r back to an m . We can insert (A.24) back into (A.20), and we get

$$\begin{aligned} \overline{q_z^{\text{cd}}}(z) &= -2 \sum_{m>0} \frac{\dot{T}_{m0}^i}{m} \cos mz - 4k \sum_{p,q>0} q \text{Im} \chi_{pq} T_{pq}^* \\ &\quad + 8k \sum_{p,q>0} q \sum_{m>0} \text{Im} \chi_{pq} T_{mq}^* \sin mz \sin pz \\ &= -2 \sum_{m>0} \frac{\dot{T}_{m0}^i}{m} \cos mz + \langle \overline{q_z} \rangle - \overline{q_z^{\text{cv}}}(z) . \end{aligned} \quad (\text{A.25})$$

So that finally we can write

$$\overline{q_z}(z) = \overline{q_z^{\text{cd}}}(z) + \overline{q_z^{\text{cv}}}(z) = \langle \overline{q_z} \rangle - 2 \sum_{m>0} \frac{\dot{T}_{m0}^i}{m} \cos mz , \quad (\text{A.26})$$

which shows that the total x -averaged vertical heat flux $\overline{q_z}$ is independent of z if the system is in a steady state, since then $\dot{T}_{m0}^i = 0$.

Bibliography

- [1] L. N. Howard and R. K. Krishnamurti, “Large-scale flow in turbulent convection: a mathematical model,” *Journal of Fluid Mechanics* **170**, 385 (1986).
- [2] S. Chandrasekhar, *Hydrodynamic and Hydromagnetic Stability* (Dover, New York, 1981).
- [3] E. L. Koschmieder, *Bénard Cells and Taylor Vortices* (Cambridge University Press, Cambridge, U.K., 1993).
- [4] G. Rüdiger, *Differential Rotation and Stellar Convection* (Akademie-Verlag, Berlin, 1989).
- [5] R. Krishnamurti and L. N. Howard, “Large-scale flow generation in turbulent convection,” *Proc. Natl. Acad. Sci. USA* **78**, 1981 (1981).
- [6] F. Wagner *et al.*, “Regime of improved confinement and high beta in neutral-beam-heated divertor discharges of the ASDEX tokamak,” *Physical Review Letters* **49**, 1408 (1982).
- [7] A. J. Wooton, B. A. Carreras, H. Matsumoto, K. McGuire, W. A. Peebles, C. P. Ritz, P. W. Terry, and S. J. Zweben, “Fluctuations and anomalous transport in tokamaks,” *Physics of Fluids B* **2**, 2879 (1990).
- [8] J. F. Drake, J. M. Finn, P. N. Guzdar, V. Shapiro, V. Shevchenko, F. Waelbroeck, A. B. Hassam, C. S. Liu, and R. Sagdeev, “Peeling of convection cells and the

- generation of sheared flows,” *Physics of Fluids B* **4**, 488 (1992).
- [9] J. M. Finn, J. F. Drake, and P. N. Guzdar, “Instability of fluid vortices and generation of sheared flows,” *Physics of Fluids B* **4**, 2758 (1992).
- [10] S. A. Orszag, “Numerical simulations of incompressible flows within simple boundaries. I. Galerkin (spectral) representations,” *Studies in Applied Mathematics* **L**, 293 (1971).
- [11] H. Sugama and C. W. Horton, “L–H confinement mode dynamics in three-dimensional state space,” *Plasma Phys. Control. Fusion* **37**, 345 (1995).
- [12] J. M. Massaguer, E. A. Spiegel, and J.-P. Zahn, “Convection-induced shears for general planforms,” *Physics of Fluids A* **4**, 1333 (1992).
- [13] J. H. Curry, “A generalized Lorenz system,” *Commun. Math. Phys.* **60**, 193 (1978).
- [14] Y. M. Treve and O. P. Manley, “Energy conserving Galerkin approximations for 2-D hydrodynamic and MHD Bénard convection,” *Physica D* **4**, 319 (1982).
- [15] J. H. Curry, J. R. Herring, J. Loncaric, and S. A. Orszag, “Order and disorder in two- and three-dimensional Bénard convection,” *Journal of Fluid Mechanics* **147**, 1 (1984).
- [16] E. N. Lorenz, “Deterministic nonperiodic flow,” *J. Atmos. Sci.* **20**, 130 (1963).
- [17] A. M. Rucklidge and P. C. Matthews, Analysis of the shearing instability in nonlinear convection and magnetoconvection, 1995, in submission.
- [18] W. H. Press, S. A. Teukolsky, B. P. Flannery, and W. T. Vetterling, *Numerical Recipes in C* (Cambridge University Press, Cambridge, U.K., 1988).

- [19] J. Prat, J. M. Massaguer, and I. Mercader, “Large-scale flows and resonances in 2-D thermal convection,” *Physics of Fluids* **7**, 121 (1995).
- [20] G. E. Willis and J. W. Deardorff, “Confirmation and renumbering of the discrete heat flux transitions of Malkus,” *Physics of Fluids* **10**, 1861 (1967).
- [21] T. H. Solomon and J. P. Gollub, “Chaotic particle transport in time-dependent Rayleigh–Bénard convection,” *Physical Review A* **38**, 6280 (1988).
- [22] S. Wiggins, *Chaotic Transport in Dynamical Systems* (Springer-Verlag, New York, 1991).
- [23] N. J. Balmforth, 1995, private communication.

Vita

Jean-Luc Thiffeault was born in Montréal, Québec, Canada on February 24, 1971, the son of Irène Thiffeault and Claude Thiffeault. After completing his work at Collège Bois-de-Boulogne, Montréal, Québec, in 1990, he entered McGill University in Montréal. He received a degree of Bachelor of Science from that school in May, 1993. In August 1993, he entered The Graduate School at the University of Texas.

Permanent address: 780 André Jobin
Ile Bizard, Québec
Canada
H9C 1W8

This thesis was typeset with L^AT_EX[†] by the author.

[†]L^AT_EX is a document preparation system developed by Leslie Lamport as a special version of Donald Knuth's T_EX Program.